

## AN OPEN-SOURCE NEUTRINO RADIATION HYDRODYNAMICS CODE FOR CORE-COLLAPSE SUPERNOVAE

EVAN O'CONNOR<sup>1,2,3</sup>*Accepted to ApJS, 2015*

## ABSTRACT

We present an open-source update to the spherically-symmetric, general-relativistic hydrodynamics, core-collapse supernova (CCSN) code GR1D (O'Connor & Ott, 2010, CQG, 27, 114103). The source code is available at <http://www.GR1Dcode.org>. We extend its capabilities to include a general relativistic treatment of neutrino transport based on the moment formalisms of Shibata et al., 2011, PTP, 125, 1255 and Cardall et al., 2013, PRD, 87 103004. We pay special attention to implementing and testing numerical methods and approximations that lessen the computational demand of the transport scheme by removing the need to invert large matrices. This is especially important for the implementation and development of moment-like transport methods in two and three dimensions. A critical component of neutrino transport calculations are the neutrino-matter interaction coefficients that describe the production, absorption, scattering, and annihilation of neutrinos. In this article we also describe our open-source, neutrino interaction library NuLib (available at <http://www.nulib.org>). We believe that an open-source approach to describing these interactions is one of the major steps needed to progress towards robust models of CCSNe and robust predictions of the neutrino signal. We show, via comparisons to full Boltzmann neutrino transport simulations of CCSNe, that our neutrino transport code performs remarkably well. Furthermore, we show that the methods and approximations we employ to increase efficiency do not decrease the fidelity of our results. We also test the ability of our general relativistic transport code to model failed CCSNe by evolving a 40 solar-mass progenitor to the onset of collapse to a black hole.

*Subject headings:* black hole physics - hydrodynamics - neutrinos - radiative transfer - stars: neutron - stars: supernovae: general

## 1. INTRODUCTION

For most massive stars with a zero-age main sequence (ZAMS) mass larger than  $8-10 M_{\odot}$ , the end of hydrostatic stellar evolution is marked by one of the most energetic events in the modern universe, a core-collapse supernova (CCSN). The cores of these massive stars become unstable to gravitational collapse when the gravitational force can no longer be balanced by the electron degeneracy pressure supplied by the electrons in the inert iron core. This marks the beginning of the core collapse phase of a CCSN. At this time, neutrinos begin to shift from being a mere sink of leptons and energy during stellar evolution to playing a much more dominant and complex role in setting the structure, dynamics, and thermodynamics of the CCSN central engine (Bethe 1990). Over 50 years of theoretical research on CCSN has revealed that an accurate treatment of neutrinos is an important and essential ingredient in modeling the CCSN central engine (Bethe & Wilson 1985; Mezzacappa & Bruenn 1993a; Liebendörfer et al. 2004; Janka et al. 2007; Ott et al. 2008; Müller et al. 2010) and the proton-neutron star cooling phase (Fischer et al. 2010; Hüdepohl et al. 2010; Roberts 2012). Furthermore, a precision treatment of neutrinos in CCSN models is needed to aid in the interpretation of neutrino signals from galactic CCSNe and the diffuse supernova neutrino background.

Energy loss due to neutrino emission, along side nuclear

dissociation, plays a large role in causing the supernova shock to initially stall. However, neutrinos are also likely a key ingredient in the ultimate shock revival. While the complete picture is still unclear, the currently most favorable scenario for this revival involves the neutrino mechanism (Bethe & Wilson 1985). The essence of the neutrino mechanism is the charged-current heating that electron-type neutrinos and anti-neutrinos emitted from deep cooling regions impose on the material behind the shock front. This heating increases the thermal energy and pressure of the matter behind the shock and it also drives convection and turbulence—all of these effects of neutrino heating enable shock expansion and aid in the transition from the initial accretion phase to the ultimate explosion phase in successful CCSNe. We refer the reader to recent reviews for full details (Janka 2012; Burrows 2013).

CCSNe and other high-energy astrophysical events like neutron star-neutron star or neutron star-black hole mergers are environments where one cannot treat neutrinos like one typically treats other particles. For example, in the central engine of CCSNe, photons, electrons, and nucleons are always in local thermodynamic equilibrium. This allows us to assume the particle distribution function and derive an equation of state (EOS) (eg. pressure, internal energy, chemical potentials, ...). Since neutrinos thermodynamically decouple from the matter at densities we are interested in studying, we cannot assume thermodynamic equilibrium as we do for other particles. In fact, it is precisely this aspect of neutrinos which gives rise to the neutrino mechanism. Neutrinos decouple from matter at one density and temperature and then non-locally transfer energy and lepton number to another re-

<sup>1</sup> North Carolina State University, Department of Physics, Campus Code 8202, Raleigh, North Carolina, USA, 27695, [evanoconnor@ncsu.edu](mailto:evanoconnor@ncsu.edu)

<sup>2</sup> CITA, Canadian Institute for Theoretical Astrophysics, Toronto, Canada, M5S 3H8

<sup>3</sup> Hubble Fellow

gion. We must model the neutrino distribution function itself to accurately simulate these astrophysical events and capture all of the essential physics.

In order to properly deal with massless neutrinos one must solve for the 7-dimensional neutrino distribution function ( $f_{\nu_i}(x^\mu, p^\alpha)$ ) as a function of time ( $x^0 = t$ ) for all spatial points ( $x^j = \vec{x}$ ), for all neutrino energies and propagation angles ( $p^\alpha = (E_{\nu_i}, \vec{p})$ ; with the restriction that  $E_{\nu_i} = |\vec{p}|$ ), and for each species ( $\nu_i$ ). The time evolution of  $f_{\nu_i}(x^\mu, p^\alpha)$  is governed by the relativistic collisional Boltzmann transport equation (Lindquist 1966),

$$p^\alpha \left[ \frac{\partial f_{\nu_i}}{\partial x^\alpha} - \Gamma_{\alpha\gamma}^\beta p^\gamma \frac{\partial f_{\nu_i}}{\partial p^\beta} \right] = \left[ \frac{df_{\nu_i}}{d\tau} \right]_{\text{coll}}, \quad (1)$$

where  $\Gamma^{\dots}$  are the Christoffel symbols and external influences including the scattering of neutrinos with other neutrinos or the surrounding matter and the absorption and emission of neutrinos by the matter (i.e., collisional processes) are apart of the collisional term,  $[df_{\nu_i}/d\tau]_{\text{coll}}$ .

In practice, solving the full time evolution of the Boltzmann equation for neutrinos in the CCSN context is a formidable task. For typical post-bounce configurations and neutrino energies, the neutrino distribution function transitions from its thermal equilibrium and isotropic value in the proton-neutron star core ( $r \lesssim 30$  km), to essentially decoupled (optical depth  $\tau \sim 0.1$ ) in the gain region ( $r \sim 100$  km) and forward peaked at distances of  $\gtrsim 200$  km (Thompson et al. 2003; Sumiyoshi & Yamada 2012). The dramatic change in the behavior of the equations from being dominated by the collision terms to being dominated by the transport terms over a short distance make the numerics particularly difficult as many approximations typically used for radiation (like the diffusion limit) are not valid everywhere. As mentioned above, the transition from the diffusive regime to the free streaming regime is absolutely crucial for the neutrino mechanism of CCSNe. It is in this region where interactions between the neutrino field and the matter are still appreciable and can lead to the development of a heating region where a net positive amount of energy can be transferred from the neutrino field to the matter. It is commonplace to make approximations to simplify the calculation from the fully relativistic 3+2+1+1 (3 spatial dimensions, 2 neutrino propagation angles, neutrino energy, and the time dimension) problem for each neutrino species down to a more tractable problem. We briefly discuss the various neutrino transport schemes used in the CCSN supernova community and discuss the advantages and disadvantages of each. We start with the most approximate and then increase in complexity of the scheme.

*Leakage Schemes:* Perhaps the crudest approximation to neutrino transport, neutrino leakage, cannot really be called a transport method at all as no evolution of the neutrino distribution function actually occurs. In general, a leakage scheme estimates the local neutrino energy and number emission rates by an interpolation between the free emission rate and the emission rate based on the diffusion approximation. This emitted energy and lepton number is then explicitly extracted from the matter. The leakage scheme used in GR1D is described in detail in O'Connor & Ott (2010). Various other examples of leakage schemes used in the high-energy astrophysics community include Ruffert et al. (1996); Rosswog & Liebendörfer (2003); Sekiguchi (2010). A disadvantage of neutrino leakage schemes in their purest form is that

they cannot self-consistently reproduce the neutrino heating. In spherically symmetric problems, or in problems that are largely spherical (like core collapse in multiple dimensions) this can be overcome by integrating the luminosity coming from smaller radii, as we have done with the leakage scheme in GR1D. However, in simulations with much less symmetry in the matter distributions (like accretion disks or compact-object mergers) this is not possible without resorting to methods like ray tracing (Perego et al. 2014).

*Moment Schemes:* An approximation often made in neutrino transport is to remove the full angular dependence of the Boltzmann transport equation by expanding the neutrino distribution function as a series of moments. The zeroth moment in this expansion is,

$$\mathcal{J}_\nu(\vec{x}, \epsilon_\nu, t) = \frac{\epsilon_\nu^3}{4\pi(hc)^3} \int_\Omega f_\nu(\vec{x}, \vec{p}, t) d\Omega, \quad (2)$$

which is a scalar quantity (the spectral energy density) that depends only on the spatial location ( $\vec{x}$ ), neutrino energy ( $|\vec{p}| = \epsilon_\nu$ ), and time ( $t$ ). This reduces the degrees of freedom from 7 to 5 (in three dimensions; 4 to 3 in spherical symmetry). This moment expansion can continue to higher moments, for example the next moment is a vector (the spectral momentum density) that depends only on the spatial location, neutrino energy, and time. Moment methods are convenient as they reduce the dimensionality of the problem resulting in fewer equations to solve. Also, the first few moments have an intuitive physical meaning and capture much of the physics in many astrophysical problems.

Within the moment scheme framework there is a lot of room for further approximations. For example, one can truncate the moment expansion at any order by specifying a *closure*, an expression that approximates the  $n+1$  moment as a function of the first  $n$  moments. The simplest variant, where one closes the moment expansion after the zeroth moment, is flux-limited diffusion (FLD). Examples in the CCSN context include Bruenn (1985) in 1D and Fryer (1999); Burrows et al. (2007); Swesty & Myra (2009); Yakunin et al. (2010); Zhang et al. (2013) in 2D. In FLD schemes, the underlying equation one solves is a diffusion equation for the neutrino energy density. A flux-limiter must be invoked that ensures the radiation does not travel faster than the speed of light in regions where the diffusion approximation fails. Similar schemes to FLD are the work of Scheck et al. (2006) and Müller & Janka (2015). In the former, the transport equation for the zeroth moment is solved in the low optical depth limit and a boundary condition is imposed at high optical depth. In the latter, an equation for the energy-dependent zeroth moment of the neutrino distribution function is solved with the help of a closure for determining the flux factor. Another FLD-like method is the isotropic diffusion source approximation (IDSA) (Liebendörfer et al. 2009) which evolves two components of the neutrino distribution function, a trapped component and a free streaming component and transfers neutrinos between these components via empirical source terms. The M1 moment scheme for neutrino radiation transport (Pons et al. 2000; Obergaulinger et al. 2014; Kuroda et al. 2012; O'Connor & Ott 2013; Just et al. 2015; Kuroda et al. 2015), evolves both the energy density and the momentum density but assumes an analytic closure for required higher moments. One can also define moment schemes where the closure is not analytic, but rather one has a variable Eddington tensor (Burrows et al. 2000; Thompson

et al. 2003; Rampp & Janka 2002; Buras et al. 2006b,a). In these cases, one uses the evolved moments as source terms to a formal integration of a Boltzmann-like equation. From this solution the higher moments (and therefore the Eddington tensor) are calculated and the system is iterated until convergence is reached. Depending on the methods used to solve for the closure, this method can be equivalent to a full Boltzmann neutrino transport calculation.

*Boltzmann Schemes:* It is also possible to solve the full Boltzmann equation taking explicitly into account both the energy and angular dependence of the neutrino distribution function. This has been done in spherical symmetry (Mezzacappa & Bruenn 1993c,a,b; Yamada 1997; Liebendörfer et al. 2004; Sumiyoshi et al. 2005), in 2D (Livne et al. 2004; Ott et al. 2008; Brandt et al. 2011), and recently in 3D (Sumiyoshi & Yamada 2012; Sumiyoshi et al. 2015). The 2D and 3D angle dependent works ignore velocity terms and do not couple the energy groups. The 3D work of Sumiyoshi & Yamada (2012); Sumiyoshi et al. (2015) is a challenging task and present results are only for static backgrounds with very low resolution in all quantities considered. The high dimensionality of Boltzmann schemes make them very expensive and simulating a three dimensional CCSN central engine with adequate resolution using this treatment is prohibitive in the foreseeable future.

*Monte Carlo Schemes:* Like many numerical problems, the transport of neutrinos can be solved by throwing computational power at the problem. For this, Monte Carlo methods for solving the Boltzmann transport equation can be used. Monte Carlo scales almost perfectly to large problem sizes and therefore is very attractive for 3D simulations. Monte Carlo methods have been used in the CCSN context for many years (Janka & Hillebrandt 1989a,b; Janka 1992; Abdikamalov et al. 2012) are potentially promising for large-scale 3D simulations in the future, although there is currently no published Monte Carlo neutrino transport work in multiple dimensions.

We note that, in principle, each of these schemes can be either energy dependent or energy independent. The latter are referred to as *grey* transport or *grey* leakage. Grey methods are computationally appealing as they remove an entire dimension of the problem. However, the energy dependence of the neutrino transport problem in the early phase of core-collapse supernovae is crucial. The cross sections of neutrinos with matter vary strongly with energy ( $\propto \epsilon^2$ ). This, in combination with the matter profiles in an accreting protoneutron star, leads to a spatial separation of the neutrinosphere locations and results in neutrino spectra that are quite non-thermal. Grey transport schemes cannot model this and therefore overestimate the number of high energy neutrinos in the gain region. In fact, early grey transport schemes in 2D were successful in obtaining explosions (Herant et al. 1994; Burrows et al. 1995; Fryer 1999) while energy dependent simulations were much less energetic (Buras et al. 2006b). This aspect of neutrino transport in core collapse warrants a multi-energy (or often referred to as multi-group) treatment of neutrinos. One of the largest deficiencies in the previous version of GR1D was its treatment of neutrinos. While the leakage/heating scheme is efficient and captures qualitative and globally quantitative aspects of the post-bounce phase, it cannot be trusted and it does not predict, for example, the emitted energy spectrum of neutrinos. In this paper, we present an implementation of

a fully general relativistic, energy dependent, multi-species neutrino radiation transport code built on the general relativistic hydrodynamics code GR1D. For each neutrino species and energy group, we evolve the first two moments of the neutrino distribution function and close the system of resulting equations via an analytic closure. We pay special attention to developing explicit methods or approximations, where possible, that will enable efficient scaling to higher dimensions. We compare our code, as well as our approximation methods, to full Boltzmann neutrino transport simulations of core collapse and several standard radiation test cases. We achieve remarkable agreement in both hydrodynamic and radiation quantities. Our complete code is available online at <http://www.gr1dcode.org>. We also make our neutrino interaction library NuLib open-source. It is available at <http://www.nulib.org>. Details of both codes pertaining to this particular paper, including the parameter files needed to reproduce all of the results of this paper are available at <http://www.stellarcollapse.org/GR1Dv2>. We encourage anyone who uses these codes to be as forthcoming with their results as we are by also providing their parameter files and any changes to the code needed to exactly reproduce their results.

In §2, we briefly summarize the hydrodynamic code GR1D and then go on to discuss in detail our new neutrino transport methods. In §3, we describe NuLib—an open-source library for neutrino interaction rates. §4 and §5 is where we test our code against several common radiation test problems and against full Boltzmann radiation transport simulations of core collapse. We also show the results of the evolution of a failed CCSN. We conclude in §6.

## 2. METHODS

### 2.1. GR1D's Hydrodynamics

Before describing our neutrino transport scheme we briefly summarize the general relativistic hydrodynamics code GR1D (O'Connor & Ott 2010). GR1D is based on the work of Romero et al. (1996) and uses the radial gauge, polar slicing metric  $g_{\alpha\beta} = \text{diag}(-\alpha^2, X^2, r^2, r^2 \sin^2 \theta)$ . In spherical symmetry, the metric coefficients can be determined directly from Hamiltonian and momentum constraints and do not have to be evolved. The  $g_{rr}$  component of the metric,  $X = 1/[1 - 2m(r)/r]^{1/2}$  is solved from an ordinary differential equation for the enclosed gravitational mass,

$$\frac{dm}{dr} = 4\pi(\rho h W^2 - P + \tau_m^r); \quad m(0) = 0, \quad (3)$$

where  $\rho$ ,  $h$ ,  $W$ , and  $P$  and the matter density, enthalpy, Lorentz factor, and pressure, respectively. The enthalpy,  $h = 1 + \epsilon + P/\rho$  contains the internal energy ( $\epsilon$ ) of the system. The Lorentz factor is related to the velocity of the fluid,  $W = 1/[1 - v^2]^{1/2}$  where following the convention of GR1D we define the fluid velocity as  $v = X v^r$ . Both the internal energy and the pressure receive contributions from the nuclear EOS, electrons, positrons, and photons. After solving for the enclosed gravitational mass, the other metric factor, the lapse ( $\alpha = \exp(\phi)$ ), can be solved for via the momentum constraint,

$$\frac{d\phi}{dr} = X^2 \left[ \frac{m}{r^2} + 4\pi r(\rho h W^2 v^2 + P + \tau_\phi^r) \right]; \quad \phi(\infty) = 0, \quad (4)$$

If we take  $\tau_{m,\phi}^\nu = 0$ , the expressions given here are for a matter only stress energy tensor. We include the contribution from neutrinos by solving Einstein's equation treating both the matter and the neutrinos as sources  $G^{\mu\nu} = 8\pi(T_{\text{matter}}^{\mu\nu} + T_{\text{neutrinos}}^{\mu\nu})$ . We delay giving an expression for  $T_{\text{neutrinos}}^{\mu\nu}$ , and therefore  $\tau_{m,\phi}^\nu$  until §2.6.3 when we are more acquainted with the moment formalism.

The hydrodynamic evolution equations are solved via the flux-conservative Valencia formulation of relativistic hydrodynamics (Font et al. 2000). The full derivation of the evolution equations used in GR1D is presented in Appendix A of O'Connor & Ott (2010), we merely present the equations here. The collection of evolution equations for the hydrodynamic variables in GR1D are,

$$\partial_t \vec{U} + \frac{1}{r^2} \partial_r \left[ \frac{\alpha r^2}{X} \vec{F}(\vec{U}) \right] = \vec{S}. \quad (5)$$

Using  $D = \rho W X$ ,  $S^r = \rho h W^2 v$ , and  $\tau = \rho h W^2 - P - D$ , the state, flux, and source vectors are defined as,

$$\vec{U} = \{D, DY_e, S^r, \tau\}, \quad (6)$$

$$\vec{F}(\vec{U}) = \{Dv, DY_e v, S^r v + P, S^r - Dv\}, \quad (7)$$

$$\vec{S} = \{0, 0, (S^r v - \tau - D)\alpha X(8\pi r P + m/r^2) + \alpha P X m/r^2 + 2\alpha P/(Xr), 0\}. \quad (8)$$

For the simulations in this paper, in GR1D, we first perform a hydrodynamic update using a second-order Runge-Kutta scheme as described in O'Connor & Ott (2010). For each substep of the Runge-Kutta, we first reconstruct  $\rho$ ,  $Y_e$ , and  $\epsilon$  to the cell edges using either the piecewise linear, total-variation-diminishing (TVD; (van Leer 1977)) minmod method (during the collapse phase) or the piecewise parabolic method (PPM Colella & Woodward 1984; after the central density reaches  $10^{12} \text{ g cm}^{-3}$ ). The intercell fluxes are determined by using these reconstructed values and the HLLC solution to the Riemann problem Einfeldt (1988). After the hydrodynamic update to the  $(n+1)$  time step is complete, we update the neutrino radiation fields from the  $(n)$  time step to the  $(n+1)$  time step using the methods described in the following section.

## 2.2. GR1D's Neutrino Transport Scheme

GR1D's neutrino transport scheme follows from the formalisms presented in Shibata et al. (2011) and Cardall et al. (2013). These formalisms differ in their derivation, however the resulting evolution equations are identical. We will rely on both formalisms in our implementation for their complementary and thorough derivations. For example, only Shibata et al. (2011) present a general casting of the neutrino source terms in terms of neutrino distribution moments while Cardall et al. (2013) fully derive the energy-coupling terms for the evolution equations. We immediately specialize the evolution equations to the metric and notation of GR1D. We forgo use of a general metric to avoid a mere restating of the derivations of Shibata et al. (2011) and Cardall et al. (2013). We hope that the simplicity of GR1D's metric, and our assumption of spherical symmetry will make the system of evolution equations clear, but general enough so that the numerical methods can easily be adapted to hydrodynamic schemes and metrics other than those GR1D and that they can be easily extended to multiple dimensions in the future.

We evolve the first two moments of the neutrino distribution function. We do this for each spatial grid point, each neutrino species, and each energy group. We express the evolution equations in the coordinate frame of GR1D while choosing the neutrino energy spectrum coordinates (neutrino energies) in the comoving frame. The latter allows the neutrino interaction terms to be determined for fixed energies regardless of the fluid velocity and then projected into the coordinate frame. We close the system of moment equations using an analytic closure. In the remainder of this section, we will present the evolution equations and discuss the numerical techniques implemented in GR1D to solve (a) the closure relation, (b) the energy-group flux term, (c) the spatial flux term, and (d) the geometric and neutrino source terms.

### 2.2.1. Radiation Moment Evolution Equations

We start by reexpressing Eqs. 171 and 172 of Cardall et al. (2013) in the notation of GR1D. This set of equations describes the evolution of the energy-dependent zeroth and first lab-frame radiation moments, the neutrino energy density ( $E$ ) and the neutrino momentum density ( $F_r$ ), respectively. We forgo a complete rederivation of this equation and point the reader to either Cardall et al. (2013) or Shibata et al. (2011).

$$\partial_t [E] + \frac{1}{r^2} \partial_r \left[ \frac{\alpha r^2}{X^2} F_r \right] + \partial_\epsilon [\epsilon(R_t + O_t)] = G_t + C_t, \quad (9)$$

$$\partial_t [F_r] + \frac{1}{r^2} \partial_r \left[ \frac{\alpha r^2}{X^2} P_{rr} \right] + \partial_\epsilon [\epsilon(R_r + O_r)] = G_r + C_r. \quad (10)$$

$R_\alpha$  and  $O_\alpha$  are terms that originate from gravitational redshifting and observer motions, respectively.  $G_\alpha$  and  $C_\alpha$  describe source terms due to geometric and matter interactions, respectively.  $P_{rr}$  is the next highest moment of the neutrino distribution function. In general the evolution equation for a given moment will always depend on higher order moments. We describe the method for calculating  $P_{rr}$ , or 'closing the system of equations' in §2.3. We explicitly note some subtle differences between the notation of Cardall et al. (2013) and our work. We evolve the energy and momentum density of a particular energy group directly, i.e. the cgs unit of  $E$  and  $F_r$  are  $\text{erg cm}^{-3} \text{ sr}^{-1} \text{ MeV}^{-1}$ , and  $\text{erg cm}^{-2} \text{ s}^{-1} \text{ sr}^{-1} \text{ MeV}^{-1}$ , respectively. Additionally, following the convention of GR1D, we evolve  $E$  and  $F_r$  rather than the densitized version  $\sqrt{\gamma}E$  and  $\sqrt{\gamma}F_r$ . This changes the geometric source terms  $G_t$  and  $G_r$ . We present our version of these expressions in §2.6.1.

For the time evolution of the neutrino moments we use a simple first-order implicit-explicit method. The spatial flux terms  $\partial_r[\alpha r^2 X^{-2} F_r]$  and  $\partial_r[\alpha r^2 X^{-2} P_{rr}]$ , as well as the energy flux terms,  $\partial_\epsilon[\epsilon(R_t + O_t)]$  and  $\partial_\epsilon[\epsilon(R_r + O_r)]$  are computed at the beginning of the neutrino radiation update using the  $(n)$  time step values of  $E$ ,  $F_r$ , and  $P_{rr}$ . Treating these flux terms as explicit, we then solve Eqs. 9 and 10 implicitly for  $E^{(n+1)}$  and  $F_r^{(n+1)}$  via,

$$\frac{E^{(n+1)} - E^{(n)}}{\Delta t} = -\frac{1}{r^2} \partial_r \left[ \frac{\alpha r^2}{X^2} F_r^{(n)} \right] - \partial_\epsilon [\epsilon(R_t^{(n)} + O_t^{(n)})] + G_t^{(n+1)} + C_t^{(n+1)}, \quad (11)$$

$$\frac{F_r^{(n+1)} - F_r^{(n)}}{\Delta t} = -\frac{1}{r^2} \partial_r \left[ \frac{\alpha r^2}{X^2} P_{rr}^{(n)} \right] - \partial_\epsilon [\epsilon(R_r^{(n)} + O_r^{(n)})] + G_r^{(n+1)} + C_r^{(n+1)}. \quad (12)$$

The explicit treatment of the flux calculations deserves special comment and will be discussed in detail in §2.4 and §2.5. The source terms will be presented in §2.6 along with the procedure for updating the conservative hydrodynamic variables at the end of the radiation step.

### 2.3. Solving for Higher Moments

For any moment expansion, the system of moment equations must be closed by assuming a closure relation for higher moments. In the evolution equation for the first moment, Eq. 10,  $P_{rr}$  represents the second moment of the lab-frame neutrino distribution function. We choose to close the system of equations here and must specify  $P_{rr}$  via a closure relation. Other second moments,  $P_\theta^\theta$  and  $P_\phi^\phi$ , as well as some third moments  $\mathcal{W}^{rrr}$ ,  $\mathcal{W}_\theta^\theta$ , and  $\mathcal{W}_\phi^\phi$  are also present in the geometric source term  $G_r$  (§2.6.1) and energy flux terms  $R_\alpha$  and  $O_\alpha$  (§2.4). We present the methods for solving for higher moments of the neutrino distribution function here. We closely follow the work of Cardall et al. (2013).

The determination of these higher moments is most easily done in the fluid frame rather than in the lab frame. This allows one to ignore contributions to the neutrino momentum from background motions of the fluid when performing the closure itself. To determine the fluid frame moments we use the neutrino stress energy tensor,  $T^{\mu\nu}$ . The fluid frame moments ( $\mathcal{J}$ ,  $\mathcal{H}^\mu$ ,  $\mathcal{K}^{\mu\nu}$ ) are the components of  $T^{\mu\nu}$  when it is expressed in a frame tied to an observer moving with a four-velocity of  $u^\mu$  (i.e. with the four-velocity of the fluid; in GR1D,  $u^\mu = [W/\alpha, Wv^r, 0, 0]$ ). Then,

$$\begin{aligned}\mathcal{J} &= u_\mu u_\nu T^{\mu\nu}, \\ \mathcal{H}^\mu &= -u_\nu h_\rho^\nu T^{\mu\rho}, \\ \mathcal{K}^{\mu\nu} &= h_\rho^\mu h_\sigma^\nu T^{\rho\sigma},\end{aligned}\quad (13)$$

where  $h_{\alpha\beta} = g_{\alpha\beta} + u_\alpha u_\beta$  is the projection operator. A similar projection of  $T^{\mu\nu}$  into the frame of an observer at rest with respect to the lab frame coordinates yields the lab-frame moments. Such an observer would have a four-velocity of  $n^\alpha$  (For completeness, in GR1D, due to the gauge choice of  $\beta^i = 0$ , the components of  $n^\alpha$  in the lab frame are:  $n^t = 1/\alpha$ ,  $n^i = 0$ ). The lab frame moment then follow as,

$$\begin{aligned}E &= n_\mu n_\nu T^{\mu\nu}, \\ F^\mu &= -n_\nu \gamma_\rho^\nu T^{\mu\rho}, \\ P^{\mu\nu} &= \gamma_\rho^\mu \gamma_\sigma^\nu T^{\rho\sigma},\end{aligned}\quad (14)$$

where  $\gamma_{\alpha\beta}$  is the spatial part of the full metric  $g_{\alpha\beta}$ . The neutrino stress energy tensor can be constructed from the zeroth, first, and second moments in any frame. In the lab frame:

$$T^{\mu\nu} = E n^\mu n^\nu + F^\mu n^\nu + F^\nu n^\mu + P^{\mu\nu}, \quad (15)$$

and in the fluid frame,

$$T^{\mu\nu} = \mathcal{J} u^\mu u^\nu + \mathcal{H}^\mu u^\nu + \mathcal{H}^\nu u^\mu + \mathcal{K}^{\mu\nu}. \quad (16)$$

The general procedure for determining the higher moments is: 1) Use the lab-frame energy ( $E$ ) and momentum density ( $F_r$ ) along with a guess for the lab-frame second moment ( $P_{rr}$ ; usually the previous value) to construct the neutrino stress energy tensor for a particular energy group via Eq. 15. 2) Determine the fluid frame moments via Eq. 13. 3) Use the analytic closure below to determine the fluid-frame second moment from

the zeroth and first moments  $\mathcal{K}^{\mu\nu}(\mathcal{J}, \mathcal{H}^\mu)$  4) Reconstruct the stress energy tensor, now with the fluid frame moments via Eq. 16, and 5) project out the lab-frame second moments via Eq. 14. Since the lab frame second moment,  $P_{rr}$ , entered into the original stress energy tensor, we must iterate this process until we reach convergence on the lab-frame second moment.

The analytic closure we apply to determine  $\mathcal{K}^{\mu\nu}$  comes from Cardall et al. (2013) Eq. 106,

$$\mathcal{K}^{\mu\nu} = \frac{\mathcal{J}}{3} h^{\mu\nu} + a(\mathcal{J}, \mathcal{H}^2) \left( \mathcal{H}^\mu \mathcal{H}^\nu - \frac{\mathcal{H}^2}{3} h^{\mu\nu} \right), \quad (17)$$

where we take  $a(\mathcal{J}, \mathcal{H}^2) = \mathcal{J}/\mathcal{H}^2 \times (3\chi - 1)/2$  with  $\mathcal{H}^2 = \mathcal{H}^\mu \mathcal{H}_\mu$ . This choice of  $a(\mathcal{J}, \mathcal{H}^2)$  gives the more commonly found form of the second moment,

$$\mathcal{K}^{\mu\nu} = \frac{3(1-\chi)}{2} \mathcal{K}_{\text{thick}}^{\mu\nu} + \frac{3\chi-1}{2} \mathcal{K}_{\text{thin}}^{\mu\nu}, \quad (18)$$

where

$$\mathcal{K}_{\text{thick}}^{\mu\nu} = \frac{\mathcal{J}}{3} h^{\mu\nu}, \quad (19)$$

is the analytic second moment derived from the diffusion limit (where the radiation field is isotropic) and

$$\mathcal{K}_{\text{thin}}^{\mu\nu} = \mathcal{J} \frac{\mathcal{H}^\mu \mathcal{H}^\nu}{\mathcal{H}^2}. \quad (20)$$

is the free streaming limit.  $\chi$  in these equations plays the role of an interpolation factor. In the optically thick limit, it asymptotes to 1/3 (giving  $\mathcal{K}^{\mu\nu} = \mathcal{K}_{\text{thick}}^{\mu\nu}$ ) and in the free streaming limit it approaches 1 (giving  $\mathcal{K}^{\mu\nu} = \mathcal{K}_{\text{thin}}^{\mu\nu}$ ). By default, GR1D uses the common choice of the Minerbo closure (Minerbo 1978; Pons et al. 2000),

$$\chi = \frac{1}{3} + \frac{2}{15} (3f^2 - f^3 + 3f^4); f = \left( \frac{\mathcal{H}^2}{\mathcal{J}^2} \right)^{1/2}, \quad (21)$$

where  $f$  is the flux factor and is a proxy for the forward peakedness of the distribution function. When  $f$  is zero the radiation field is isotropic. When  $f$  is one, the radiation field is completely forward peaked in the direction of the neutrino momentum.

For the analytic fluid frame third moments ( $\mathcal{L}^{\mu\nu\rho}$ ) we use, Eq. 108 from Cardall et al. (2013) taking  $b(\mathcal{J}, \mathcal{H}) = 1/\mathcal{H}^2 \times (3\chi - 1)/2$ ,

$$\mathcal{L}^{\mu\nu\rho} = \frac{3(1-\chi)}{2} \mathcal{L}_{\text{thick}}^{\mu\nu\rho} + \frac{3\chi-1}{2} \mathcal{L}_{\text{thin}}^{\mu\nu\rho}, \quad (22)$$

where

$$\mathcal{L}_{\text{thick}}^{\mu\nu\rho} = \frac{1}{5} (\mathcal{H}^\mu h^{\nu\rho} + \mathcal{H}^\rho h^{\mu\nu} + \mathcal{H}^\nu h^{\mu\rho}), \quad (23)$$

and

$$\mathcal{L}_{\text{thin}}^{\mu\nu\rho} = \frac{\mathcal{H}^\mu \mathcal{H}^\nu \mathcal{H}^\rho}{\mathcal{H}^2}. \quad (24)$$

From this, we compute the lab frame third moments, denoted here as  $\mathcal{W}^{\mu\nu\rho}$ , via Eq. B18 of Cardall et al. (2013). The moments relevant for GR1D are

$$\mathcal{W}^{rrr} = \mathcal{L}^{rrr} + 3 \left( \frac{Wv}{X} \right) \mathcal{K}^{rr} + 3 \left( \frac{Wv}{X} \right)^2 \mathcal{H}^r + \left( \frac{Wv}{X} \right)^3 \mathcal{J}, \quad (25)$$

and

$$\overline{\mathcal{W}^{r\phi}} = \mathcal{L}^{r\phi} + \left(\frac{Wv}{X}\right) \mathcal{K}^\phi_\phi. \quad (26)$$

#### 2.4. Methods for Coupling Energy Groups

The components of the energy flux terms,  $R_\alpha$  and  $O_\alpha$  from Eqs. 9 and 10, are given in Cardall et al. (2013) and reproduced here using the metric and notation of GR1D.

$$R_t = \alpha W \left[ \left(\frac{\mathcal{Z}v}{X} - \mathcal{Y}^r\right) \partial_r \phi - \frac{\mathcal{X}^{ii}v}{2X} \partial_r g_{ii} + \mathcal{X}^{rr} K_{rr} \right], \quad (27)$$

$$O_t = \alpha \left[ \frac{\mathcal{Z}}{\alpha} \partial_t W + \mathcal{Y}^r \partial_r W - \frac{\mathcal{Y}_r}{\alpha} \partial_t \frac{Wv}{X} - \mathcal{X}_r^r \partial_r \frac{Wv}{X} \right], \quad (28)$$

and

$$R_r = \alpha W \left[ \left(\frac{\mathcal{Y}_r v}{X} - \mathcal{X}_r^r\right) \partial_r \phi - \frac{\mathcal{W}_r^{ii}v}{2X} \partial_r g_{ii} + \mathcal{W}_r^{rr} K_{rr} \right], \quad (29)$$

$$O_r = \alpha \left[ \frac{\mathcal{Y}_r}{\alpha} \partial_t W + \mathcal{X}_r^r \partial_r W - \frac{\mathcal{X}_{rr}}{\alpha} \partial_t \frac{Wv}{X} - \mathcal{W}_{rr} \partial_r \frac{Wv}{X} \right], \quad (30)$$

where

$$W\mathcal{Z} = E + \frac{vF_r}{X} + \frac{v^2 P_{rr}}{X^2} + \frac{Wv^3}{X^3} \mathcal{W}_{rrr}, \quad (31)$$

$$W\mathcal{Y}^r = \frac{F_r}{X^2} + \frac{vP_{rr}}{X^3} + \frac{Wv^2}{X^4} \mathcal{W}_{rrr}, \quad (32)$$

$$W\mathcal{X}^{rr} = \frac{P_{rr}}{X^4} + \frac{Wv}{X^5} \mathcal{W}_{rrr}, \quad (33)$$

$$W\mathcal{X}^{\theta\theta} = \frac{P_\theta^\theta}{r^2} + \frac{Wv}{Xr^2} \mathcal{W}_{r\theta}^\theta, \quad (34)$$

$$W\mathcal{X}^{\phi\phi} = \frac{P_\phi^\phi}{r^2} + \frac{Wv}{Xr^2} \mathcal{W}_{r\phi}^\phi. \quad (35)$$

$K_{rr} = -X\dot{X}/\alpha$  (not to be confused with  $\mathcal{K}^{\mu\nu}$ ) in Eqs. 27 and 29 is the extrinsic curvature. Required radial and time derivatives of the metric quantities are analytic in the metric of GR1D and available in O'Connor & Ott (2010). For the radial and time derivatives of the velocity we use finite differencing,  $\dot{v} = (v^{(n+1)} - v^{(n)}) / (t^{(n+1)} - t^{(n)})$  and  $dv_i/dr = (v_{i+1} - v_{i-1}) / (x_{i+1} - x_{i-1})$ .

For determining the inter-group fluxes we follow the number-conserving scheme of Müller et al. (2010). This scheme computes the momentum space fluxes via the equations presented here and reconstructs the flux at the energy group interface by assigning weights to the left and right states. The weights are determined in such a way as to conserve neutrino number. GR1D can treat these energy group couplings implicitly or explicitly. Due to the small time step enforced via the spatial flux treatment (see the following section), we find an explicit treatment of these terms is sufficient for typical situations and avoids a large matrix inversion.

#### 2.5. Explicit Update for the Spatial Flux

The transport of neutrinos from one spatial zone to another is handled via the spatial flux term in Eqs. 9 and 10. We solve these terms with the standard hyperbolic methods used for conservative hydrodynamics and apply asymptotic solutions

for the optically thick regimes where the hyperbolic methods fail.<sup>4</sup>

We base the spatial flux term calculation on the methods used in the HLLC (Einfeldt 1988) Riemann solver. First, the lab-frame moments are reconstructed to the left and right sides of the cell interface. In GR1D we adopt the same reconstructor we use for the hydrodynamics, either TVD (for the collapse phase) or piecewise parabolic (once the density has reached  $10^{12} \text{ g cm}^{-3}$ ). For non core collapse test cases in this paper, we use TVD. In practice, we reconstruct the zeroth moment ( $E$ ) and the ratio of the first moment to the zeroth moment ( $F_r/E$ ) to insure that  $F_r/E$  at the interface never exceeds the value in the zone center and therefore remains casual. The closure is re-solved to obtain the interface values of the second moment in the lab-frame. Following Shibata et al. (2011), we estimate the characteristic speeds needed in the Riemann solution via an interpolation between the optically thick and free streaming regimes,

$$\lambda^{\max/\min} = \frac{3(\chi-1)}{2} \lambda_{\text{thick}}^{\max/\min} + \frac{3\chi-1}{2} \lambda_{\text{thin}}^{\max/\min}, \quad (36)$$

where  $\chi$  is computed as part of the closure (see §2.3),

$$\lambda_{\text{thick}}^{\max/\min} = \max/\min(\alpha X \frac{2W^2v \pm \sqrt{3}}{2W^2+1}, \alpha Xv), \quad (37)$$

and

$$\lambda_{\text{thin}}^{\max/\min} = \max/\min(\pm \alpha X). \quad (38)$$

The inter-cell fluxes from the Riemann solution are then given as

$$F_r^{i+1/2, \text{HLLC}} = \frac{\lambda^{\max} F_r^{i,R} - \lambda^{\min} F_r^{i+1,L} + \lambda^{\max} \lambda^{\min} (E^{i+1,L} - E^{i,R})}{\lambda^{\max} - \lambda^{\min}}, \quad (39)$$

and

$$P_{rr}^{i+1/2, \text{HLLC}} = \frac{\lambda^{\max} P_{rr}^{i,R} - \lambda^{\min} P_{rr}^{i+1,L} + \lambda^{\max} \lambda^{\min} (F_r^{i+1,L} - F_r^{i,R})}{\lambda^{\max} - \lambda^{\min}}, \quad (40)$$

where  $A^{i,R/L}$  are the reconstructed moments to the right/left interface in zone  $i$ . In the optically thick regime, or what we refer to as the high Peclet number regime ( $\text{Pe} \sim (\Delta x_i \times \kappa_i)$ ; or the optical depth of the zone  $i$ ), the diffusive term in the Riemann solution becomes dominated by numerical noise and is no longer accurate (Audit et al. 2002). In these regions we replace the interface fluxes by their asymptotic values. In GR1D, the  $\mathcal{O}(v/c)$  approximation for this asymptotic flux is (Roberts 2014)

$$F_r^{i+1/2, \text{asym}} = \frac{4W^2vX}{3} \mathcal{J} - \frac{W}{3\bar{\kappa}X^2} \frac{\partial \mathcal{J}}{\partial r}, \quad (41)$$

where the first term is the flux due to advection with the fluid, and the second term is the flux due to diffusion. For the advection we use an explicit upwind scheme. We estimate  $\partial \mathcal{J} / \partial r$  via a simple finite difference of the fluid frame energy densities. For the momentum flux in the high Peclet number regime, we take a simple average of the neighboring zone's second moment for the asymptotic flux,

$$P_{rr}^{i+1/2, \text{asym}} = (P_{rr}^i + P_{rr}^{i+1}) / 2. \quad (42)$$

<sup>4</sup> We are indebted to Luke Roberts for many discussions on this topic and for the ultimate  $\mathcal{O}(v/c)$  solution in GR1D.

We interpolate between the two regimes using the Peclet number. Following Jin & Levermore (1996); Audit et al. (2002),

$$a = \tanh(1/\overline{\text{Pe}}), \quad (43)$$

where  $\overline{\text{Pe}} = \sqrt{(\kappa_s^i + \kappa_a^i)(\kappa_s^{i+1} + \kappa_a^{i+1})}(x_{i+1} - x_i)W^3(1+\nu)X^2$  and  $\kappa_s$  and  $\kappa_a$  are the scattering and absorption opacities, respectively. The extra  $W^3(1+\nu)X^2$  terms arise from the coefficients of the neutrino momentum sink term in  $C_r$  (see §2.6 and Audit et al. 2002).  $a = 1$  in regions of small Peclet number,  $a \propto 1/\text{Pe}$  in regions with large Peclet number, and the tanh function gives a smooth interpolation in between. The ultimate value for the fluxes on the cell interfaces is,

$$F_r^{i+1/2} = a \times F_r^{i+1/2, \text{HLL E}} + (1-a) \times F_r^{i+1/2, \text{asym}}, \quad (44)$$

and

$$P_r^{i+1/2} = a \times P_{rr}^{i+1/2, \text{HLL E}} + (1-a) \times P_{rr}^{i+1/2, \text{asym}}. \quad (45)$$

The flux update terms in the moment evolution equations are taken to be

$$\partial_r \left[ \frac{\alpha r^2}{X^2} F_r^{(n)} \right] = \frac{1}{\Delta r^i} \left\{ \left[ \frac{\alpha r^2}{X^2} \right]^{i+1/2} F_r^{i+1/2} - \left[ \frac{\alpha r^2}{X^2} \right]^{i-1/2} F_r^{i-1/2} \right\}, \quad (46)$$

and

$$\partial_r \left[ \frac{\alpha r^2}{X^2} P_{rr}^{(n)} \right] = \frac{1}{\Delta r^i} \left\{ \left[ \frac{\alpha r^2}{X^2} \right]^{i+1/2} P_{rr}^{i+1/2} - \left[ \frac{\alpha r^2}{X^2} \right]^{i-1/2} P_{rr}^{i-1/2} \right\}. \quad (47)$$

The CFL condition restricts the maximum time step that can be taken to the light crossing time of the smallest spatial zone. Additionally, we reduce the time step via a Courant factor of 0.5. In GR1D, this sets the time step for both the hydrodynamic step and the neutrino radiation step. While the hydrodynamic step uses a second-order Runge-Kutta for the time evolution, the neutrino radiation step uses a simpler first order scheme for both the implicit and explicit parts. While first-order explicit methods are normally not used because they are very inaccurate, two aspects alleviate this issue in GR1D. GR1D generally uses a logarithmically spaced grid. The innermost zones are  $\mathcal{O}(200m)$  and these set the time step. However, in these zones the radiation is generally optically thick and therefore the fluxes do not have characteristic speeds close to the speed of light. For the free streaming regions farther out, the speeds are close to the speed of light, however, due to the logarithmic spacing, these zones are much larger than the smallest zone. The only place where there is nearly free streaming radiation closer to the innermost zones is near bounce when the extent of the supersonic flow reaches down to  $\sim 10\text{km}$ . For this reason, and because the epoch of core bounce is very dynamic, we decrease the Courant factor to 0.25 when the central density first reaches  $10^{12} \text{g cm}^{-3}$ . We increase the Courant factor back to 0.5 at 20 ms after core bounce. At times other than near core bounce, we do not see differences when decreasing the Courant factor below 0.5. This give us confidence that this treatment is sufficient for accurate evolutions.

## 2.6. Source terms

The neutrino radiation fields are sourced and sinked by weak interaction processes occurring in the matter, between

the neutrinos and the matter, or between the neutrinos themselves. There are also geometric source terms that arise due to our particular set of evolution equations. GR1D can currently handle most types of standard neutrino-matter interactions. In this section, we will discuss these types of interactions and how they are included in both the neutrino and hydrodynamic evolution equations. In the following section we introduce NuLib, an open-source neutrino interaction library and describe the specific neutrino-matter interactions it includes.

### 2.6.1. Geometric Source Terms

The geometric source terms,  $G_\alpha$  in Eqs. 9 and 10 are given in both Cardall et al. (2013) and Shibata et al. (2011), we repeat them here in the notation and metric of GR1D. We note that the differences in the definition of the evolved variables between GR1D and these other works affects the definitions of  $G_t$  and  $G_r$  (i.e. GR1D evolves  $E$  and  $F_r$  as opposed to the densitized versions,  $\sqrt{\gamma}E$  and  $\sqrt{\gamma}F_r$  where  $\gamma$  is the determinant of the metric). The geometric source term for the zeroth neutrino moment is

$$G_t = \alpha 4\pi r \rho h W^2 [E\nu X(1+p_{rr}/X^2) - F_r(1+\nu^2)], \quad (48)$$

where  $p_{rr} = P_{rr}/E$  is the Eddington factor and  $h$  is the enthalpy defined in §2.1. While the geometric source term for the momentum density is

$$G_r = -\alpha 4\pi r \rho h W^2 F_r \nu X - \alpha E X^2 \left[ \frac{m}{r^2} + 4\pi r (P + \rho h W^2 \nu^2) \right] + \alpha E \frac{P_\phi^\theta + P_\theta^\theta}{r}, \quad (49)$$

where  $p^i = P_i/E$  and we note that  $P$  is the matter pressure and  $m$  is the enclosed mass given by Eq. 3.

### 2.6.2. Neutrino Source Terms

For the neutrino-matter interaction source terms we follow the source term formalism of Shibata et al. (2011). The neutrino source terms in Eqs. 9 and 10 are,

$$C_t = -\alpha n_\alpha \left[ S_{e/a}^\alpha + S_{\text{iso}}^\alpha + S_{\text{scatter}}^\alpha + S_{\text{thermal}}^\alpha \right], \quad (50)$$

and

$$C_r = \alpha \gamma_{r\alpha} \left[ S_{e/a}^\alpha + S_{\text{iso}}^\alpha + S_{\text{scatter}}^\alpha + S_{\text{thermal}}^\alpha \right], \quad (51)$$

where  $S_{e/a}^\alpha$  is the source term for emission and absorption of neutrinos from and into the matter, respectively,  $S_{\text{iso}}^\alpha$  is the source term for elastic scattering of neutrinos off the matter,  $S_{\text{scatter}}^\alpha$  encompasses the source term for inelastic scattering of neutrinos off matter, and  $S_{\text{thermal}}^\alpha$  describes thermal production of neutrino-antineutrino pairs and their annihilation. These terms are expressed most easily in the fluid rest frame and will be functions of  $\mathcal{J}$ ,  $\mathcal{H}^\alpha$ ,  $\mathcal{K}^{\alpha\beta}$ , the fluid four-velocity  $u^\alpha$ , and the neutrino-matter interaction coefficients. For solving the implicit step, it is necessary to know the neutrino source terms in terms of the lab frame moments  $E$ ,  $F_r$ , and the closure relations of §2.3. Using Eqs. 13 and 15, it is easily possible to show that in GR1D,

$$\mathcal{J} = W^2 [E - 2F_r \nu / X + P_{rr} \nu^2 / X^2], \quad (52)$$

and

$$\mathcal{H}^t = \frac{W^3}{\alpha} [-(E - F_r v/X)v^2 + vF_r/X - v^2 P_{rr}/X^2], \quad (53)$$

$$\mathcal{H}^r = W^3 [-(E - F_r v/X)v/X + F_r/X^2 - vP_{rr}/X^3]. \quad (54)$$

When we perform the implicit solve for  $E^{(n+1)}$  and  $F_r^{(n+1)}$  we assume  $P_{rr}^{(n+1)} = p_{rr}^{(n)} E^{(n+1)}$ . Since we first solve the hydrodynamic step before the radiation step, we have an estimate of  $\rho^{(n+1)}$ ,  $T^{(n+1)}$ , and  $Y_e^{(n+1)}$ . We use these to determine the neutrino interaction terms. We do not include  $T$  and  $Y_e$  in the implicit solution (and therefore do not recalculate these interaction coefficients when finding the solution), rather we update them once after we solve for  $E^{(n+1)}$  and  $F_r^{(n+1)}$ . These approximations are justified since, unlike most implicit schemes, we are limited to very small time steps from the explicit spatial flux calculation (see §2.5).

From Shibata et al. (2011),

$$S_{e/a}^\alpha = [\eta - \kappa_a \mathcal{J}] u^\alpha - \kappa_a \mathcal{H}^\alpha, \quad (55)$$

where  $\eta$  is the emissivity and  $\kappa_a$  is the absorption opacity for neutrinos of a given species and energy. Weak interactions that produce neutrinos (such as electron capture on protons) and destroy neutrinos (such as the inverse interaction of electron neutrino capture on neutrons) are used to compute  $\eta$  and  $\kappa_a$ . We describe this in more detail in §3 on NuLib.

$$S_{\text{iso}}^\alpha = -\kappa_s \mathcal{H}^\alpha, \quad (56)$$

where  $\kappa_s$  is the scattering opacity for neutrinos of a given species and energy. Only isoenergetic (elastic) interactions where the neutrino survives the interaction with the same energy as it started will contribute to this scattering opacity.

These first two neutrino source terms were mono-energetic. They do not depend on the neutrino distribution function of other neutrino species or energies.  $S_{\text{scatter}}^\alpha$  is more complicated since it depends on the neutrino distribution function at all other neutrino energies. The inelastic neutrino-matter scattering opacity depends on the occupation level of the final state neutrino. If that energy level is completely filled with other neutrinos than the scattering is blocked. Therefore, at a given energy, we must consider the scattering to every other neutrino energy individually and take into account the neutrino phase space occupancy of that energy group. This process couples all of the energy bins for a given species and can dramatically increase the required computational resources if many energy groups are considered. To avoid a mere restatement of complex formulas, we refer the reader to Shibata et al. (2011) for specific definitions of  $S_{\text{scatter}}^\alpha$  (their Eq. 4.14) but note the slight notation differences between our work and their's *a*) their  $L^{\alpha\beta}$  is our  $\mathcal{K}^{\alpha\beta}$ , *b*) their fluid frame moments are also integrated over solid angle and therefore are  $4\pi$  larger than ours. We discuss the scattering kernels ( $R_{0/1}^{\text{in/out}}$ ) calculation in NuLib in the following section.

Since the full implicit calculation of inelastic scattering is computationally demanding, any potential simplification and/or approximation is greatly desired. In the context of CCSN simulations in GR1D, we have found that we can forgo the full implicit inelastic neutrino-electron scattering calculation and instead include this interaction as an explicit term in Eqs. 9 and 10. This works in part because of the small time step afforded to us from the explicit flux calculation. However, in order to achieve a stable evolution when the time

scale of inelastic scattering is shorter than our time step, we must decrease the magnitude of the scattering kernels that enter into  $S_{\text{scatter}}^\alpha$ . Following inspiration from Thompson et al. (2003), we have empirically found that suppressing the scattering kernels at densities above  $\rho = 5 \times 10^{12} \text{ g cm}^{-3}$  via,

$$R_{0/1}^{\text{in/out},*} = R_{0/1}^{\text{in/out}} / \max[1, (\rho / (5 \times 10^{12} \text{ g cm}^{-3}))^{3/2}], \quad (57)$$

is sufficient. This effectively slows down the scattering of the neutrinos in these high density regimes and will likely be invalid when the neutrinosphere reaches these densities. In §5.2, we show that there are no serious side effects of this approximation for a typical early-phase CCSN in GR1D.

The last main group of neutrino interactions are neutral current pair-process interactions or thermal interactions. They enter into the term  $S_{\text{thermal}}^\alpha$  in Eqs. 50 and 51. These are processes that produce neutrino-antineutrino pairs through, for example, electron-positron annihilation. A fully consistent treatment of these processes requires coupling neutrino species as well as energy groups. We leave this for future work and treat these processes in GR1D via an approximation<sup>5</sup>. We approximate the neutrino-antineutrino annihilation rate via an interpolation between the limiting regimes. We assign an absorption opacity to this interaction via  $\kappa_a^{pp} = \eta^{pp} / B_\nu$  where  $\eta^{pp}$  is the isotropic emissivity of neutrinos due to some thermal process (i.e. electron-positron annihilation) assuming no final state neutrino blocking and  $B_\nu$  is the neutrino black-body function for that density, temperature and electron fraction. This ensures both the correct emission rate when there are no neutrinos present to block neutrino-antineutrino production and it ensures that in equilibrium (when  $\mathcal{J} = B_\nu$ ) there is no net emission since  $\eta^{pp} - \kappa_a^{pp} \mathcal{J}$  will be zero by construction. By default, we use this approximation for producing and ‘annihilating’  $\nu_x$  neutrinos in GR1D. Furthermore, we ignore thermal processes for electron type neutrino and antineutrinos because the production of these neutrinos is dominated by charged current processes over pair-production processes. For CCSNe, we find that our heavy-lepton production/annihilation approximation is highly successful giving comparable neutrino signals to an implicit solution. (see §5.1 and §5.2 for details, but we find luminosities within  $\sim 7\%$  and root mean squared energies within  $\sim 2\%$ ).

### 2.6.3. Neutrino-Matter coupling

The neutrino-matter source terms are also source terms for the matter evolution equations. They can influence the energy content, the lepton content, and the momentum of the matter. We update the conservative hydrodynamic variables (from Eq. 6) at the end of the neutrino radiation step with the corresponding change to the neutrino variables<sup>6</sup>. This ensures any energy, leptons, or momentum sourced into the neutrino

<sup>5</sup> However, we carry out several simulations in §5.2 where we treat  $\nu_x \bar{\nu}_x$  production/annihilation via electron-positron annihilation/production fully (via Shibata et al. (2011)’s methods) to test this approximation. As we do not yet do this for electron type neutrinos, or for other processes like nucleon-nucleon Bremsstrahlung, we leave a formal discussion of it to future work.

<sup>6</sup> This is different from most fully implicit methods where the matter coupling is also included in the implicit step. Since our time step is forced to be small by the light crossing time of the smallest zone, we find that coupling the matter into the implicit source term step is not necessary.

fields is subtracted from the matter.

$$\Delta[\tau] = -\Delta t \times 4\pi\alpha^2 \sum_{\epsilon, \nu_i} S^t, \quad (58)$$

$$\Delta[S_{\text{hydro}}^r] = -\Delta t \times 4\pi\alpha X \sum_{\epsilon, \nu_i} S^r, \quad (59)$$

$$\Delta[DY_e] = -\Delta t \times 4\pi\alpha X m_N \sum_{\epsilon, \nu_i} s_{\nu_i} W [S^t \alpha - S^r X \nu] / \epsilon, \quad (60)$$

where  $\Delta t$  is the numerical time step,  $S^t$  and  $S^r$  are the source terms in Eqs. 50 and 51 evaluated in the lab frame and  $s_{\nu_i}$  denotes lepton number: 1 for  $\nu_e$ , -1 for  $\bar{\nu}_e$ , and 0 for  $\nu_x$ . For  $\Delta[\tau]$  and  $\Delta[S_{\text{hydro}}^r]$ , the preceding factors of  $\alpha^2$  and  $\alpha X$  arise from Eqs. 50 and 51, respectively. We note that there is a subtle factor of  $X$  between the definitions of the conserved hydro quantity  $S_{\text{hydro}}^r$  and the neutrino momentum  $F_r$  such that the sum of  $\Delta[S_{\text{hydro}}^r X + F_r] = 0$  (see Appendix A of O'Connor & Ott 2010 for details of the precise definition of  $S_{\text{hydro}}^r$ ). Since the neutrino energies are defined in the fluid rest frame, the lepton number change must be computed from the energy source term in that frame (i.e. rather than taking  $s_{\nu_i} S^t / \epsilon$  as the lepton source term). Therefore, for the definition of  $\Delta[DY_e]$  in Eq. 60, the calculation could also be carried out with the more intuitive  $[\eta - \kappa_a \mathcal{J}] / \epsilon$  instead of the more cumbersome  $W[S^t \alpha - S^r X \nu] / \epsilon$ . These expressions are equivalent as can be shown via Eq. 53 - Eq. 56. Finally, we note that  $S_{\text{scatter}}^\alpha$  and  $S_{\text{thermal}}^\alpha$  will contribute to both Eq. 58 and Eq. 59, but not to Eq. 60.

The other neutrino-matter coupling is through the gravitational field and we are now in a position to derive the neutrino contributions to the metric equations alluded to in Eqs. 3 and Eq. 4. The neutrino stress energy tensor is simply the energy integrated form of Eq. 15 or Eq. 16,

$$T_{\text{neutrino}}^{\mu\nu} = 4\pi \sum_{\text{species } i} \sum_{\text{energy } \epsilon} T_{i,\epsilon}^{\mu\nu} \Delta\epsilon. \quad (61)$$

While both give the correct contribution, we choose to use the lab-frame representation of the neutrino stress energy tensor, Eq. 15. This gives (Gourgoulhon 1991),

$$\tau_m^\nu = -T_{\text{neutrino}}^t = 4\pi \sum_{\text{species } i} \sum_{\text{energy } \epsilon} E_{i,\epsilon} \Delta\epsilon, \quad (62)$$

$$\tau_\phi^\nu = -T_{\text{neutrino}}^r = 4\pi \sum_{\text{species } i} \sum_{\text{energy } \epsilon} P_{i,\epsilon}^r \Delta\epsilon. \quad (63)$$

### 3. NEUTRINO MICROPHYSICS: NULIB

The neutrino-matter interaction coefficients introduced in §2.6 contain contributions from many different processes. These coefficients depend directly on the matter density,  $\rho$ ; temperature,  $T$ ; matter chemical potentials,  $\mu_e$ ,  $\mu_n$ ,  $\mu_p$ ; and the nuclear isotope distribution and therefore require an EOS to compute. They also strongly depend on neutrino energy and species. Similar to what is done for nuclear EOS, for matter in nuclear statistical equilibrium we can precompute all the neutrino-matter interaction coefficients and tabulate them for quick, on the fly *interpolation* rather than the slower on the fly *computation*. While table interpolation has the benefit of speeding up the determination of the neutrino interaction rates, there can be consequences of this if the interpolation does not follow inherent relationships between quantities, we

**Table 1**  
Neutrino Interactions in NuLib

Production	
Charged-Current Interactions	Thermal Processes
$\nu_e + n \rightarrow p + e^-$	$e^- + e^+ \rightarrow \nu_x + \bar{\nu}_x$
$\bar{\nu}_e + p \rightarrow n + e^+$	$N + N \rightarrow N + N + \nu_x + \bar{\nu}_x$
$\nu_e + (A, Z) \rightarrow (A, Z+1) + e^-$	
Scattering	
Iso-Energetic Scattering	Inelastic Scattering
$\nu + \alpha \rightarrow \nu + \alpha$	$\nu_i + e^- \rightarrow \nu_i' + e^{-\prime}$
$\nu_i + p \rightarrow \nu_i + p$	
$\nu_i + n \rightarrow \nu_i + n$	
$\nu + (A, Z) \rightarrow \nu + (A, Z)$	

**Note.** — Neutrino interactions from NuLib used in this study. Production interactions with neutrinos on the left are computed as cross sections, production interactions with neutrinos on the right are computed as emissivities. Interactions with  $\nu$  are not flavor sensitive, while interactions with  $\nu_i$  are. Specific interactions that only involve one type of neutrino use the specific neutrino flavor.  $\nu_x$  is used to denote heavy-lepton neutrinos.

note a few of these situations below when discussing various processes.

The collection of routines we use to compute the neutrino-matter interaction coefficients for GR1D is called NuLib. NuLib is an open-source library and available as a git repository at <http://www.nulib.org>. We have tagged a release called ‘GR1Dv2’ to accompany this paper. We summarize the rates included in the simulations of this paper from NuLib in Table 1 and discuss details below. Every rate and correction in NuLib is optional and can easily be left out of the calculation for the total rate. For a full description of the neutrino interactions and their implementation, please consult documentation and source code at <http://www.nulib.org>. The set of available interactions is constantly evolving. Contributions to this community resource are welcome.

*Absorption Cross Sections:* NuLib’s neutrino-nucleon charged-current interaction cross sections are taken from Burrows et al. (2006). Weak-magnetism and recoil corrections from Horowitz (2002) are applied. NuLib also includes neutrino absorption on heavy nuclei via the simple treatment of Burrows et al. (2006); Bruenn (1985). More complete electron capture rates on heavy nuclei will be included in a future version of NuLib. Cross sections are converted to opacities using the target number densities from the chosen EOS. Emissivities are computed via Kirchhoff’s Law, which equates the neutrino emission rate to the absorption rate of an equilibrium distribution of neutrinos. This does not require the neutrinos to be in equilibrium and is valid regardless of the background neutrino field. We note that table interpolation is not guaranteed to maintain this relationship between the emissivity and opacity. In practice, in GR1D, we enforce this relationship by recomputing the emissivity from the absorption opacity after interpolation.

*Thermal Neutrino Pair Production:* For thermal processes, NuLib makes the approximation mentioned in §2.6.2. We compute the emissivity assuming there is no final state neutrino blocking. For electron-positron annihilation, this calculation is only a function of the electron chemical potential and matter temperature since this completely sets the electron and positron distributions. We compute the emissivity following Burrows et al. (2006); Bruenn (1985) which is based on the earlier work of Yueh & Buchler (1976). We com-

pute the zeroth moment of the neutrino production kernels to get the total energy emission. We assume it is isotropic. For nucleon-nucleon Bremsstrahlung we also follow Burrows et al. (2006) and make the same assumption we make for electron-positron annihilation. NuLib also computes the zeroth and first moment of the neutrino production/annihilation kernels for electron-positron annihilation. This allows us to test the quality of our approximation. We present the results of that test in §5.2.

*Elastic Scattering:* For elastic scattering processes we include scattering off nucleons, alpha particles, and heavy nuclei following Bruenn (1985); Burrows et al. (2006). For elastic scattering on nucleons we include weak magnetism and recoil corrections from Horowitz (2002). For coherent scattering on heavy nuclei we follow the implementation from Burrows et al. (2006). These rates use the average nuclear mass ( $\bar{A}$ ) and average nuclear charge ( $\bar{Z}$ ) from the EOS and include form factor corrections due to decoherence and an electron polarization correction. They also include ion-ion correlations from Horowitz (1997). Elastic scattering off  $\alpha$  particles uses the heavy nuclei scattering cross section with  $A = 4, Z = 2$ , but drops the corrections.

*Inelastic Neutrino-Electron Scattering:* NuLib calculates the zeroth and first moment of the neutrino-electron scattering kernel as computed in Bruenn (1985). These kernels are computed as a function of electron chemical potential (or specifically,  $\eta_e = \mu_e/T$ ), temperature, and both incoming and outgoing neutrino energy. In GR1D, after interpolation, we enforce the in/out symmetry of the scattering kernels  $R_\ell^{\text{in}}(\epsilon', \epsilon) = R_\ell^{\text{out}}(\epsilon, \epsilon')$  as well as  $R_\ell^{\text{out}}(\epsilon, \epsilon') = \exp[-(\epsilon' - \epsilon)/T] \times R_\ell^{\text{out}}(\epsilon', \epsilon)$  (Chernohorsky 1994). This has the added benefit of reducing the number of interpolations needed.

This set of interactions is motivated by and is equivalent to the set used in Liebendörfer et al. (2005), with the exception that NuLib includes weak-magnetism and recoil corrections. In the CCSN test problems that follow in §5.1 we use this set of interactions, ignoring the weak-magnetism and recoil corrections for the sake of comparison. This set is in no way complete, or even modern. More complete neutrino interaction rates are available in the literature, most notably inelastic neutrino-nucleon scattering (Reddy et al. 1998), and electron capture rates on heavy nuclei (Langanke et al. 2003).

#### 4. RADIATION TEST PROBLEMS

In this section we rigorously test our transport implementation against classic radiation test problems. We begin with several classical radiating spheres in §4.1 and move on to gravitating radiating spheres with a background fluid motion in §4.2. In §4.3, we further test our explicit flux treatment by performing a diffusion wave test.

##### 4.1. Classical Radiation Spheres

We perform two classical radiating sphere tests. In both tests the sphere has a radius of 1 and there is no scattering opacity. The first test is one where the absorption opacity is chosen such that the optical depth in the center of the sphere is very large,  $\tau = 250$ , with a very coarse grid (100 evenly spaced zones out to a radius of 5) such that the Peclet number is  $\text{Pe}=12.5$  for cells interior to the radiating sphere. The corrections we impose on the explicit fluxes dominate for this

test. The value of  $a$  in Eq. 43 is  $\sim 0.08$  for zones inside the sphere and 1 outside. The matter interaction variables follow from Abdikamalov et al. (2012) ( $b = 10; \kappa_a = 250; r_{\text{surface}} = 1$ ). The second radiating sphere is more optically thin. The opacity is chosen such that the optical depth in the center of the sphere is 4. This test uses a very fine grid (800 evenly spaced zones out to a radius of 3) such that the Peclet number for interior zones is  $\text{Pe}=0.015$ . The corrections are non-existent,  $a$  in this case is 1 everywhere. The matter interaction variables follow from Smit et al. (1997) ( $b = 0.8; \kappa_a = 4, r_{\text{surface}} = 1$ ). For both cases, analytic solutions exist (see Smit et al. 1997). In Fig. 1 we show the results of these two tests using GR1D (dashed lines) along with the analytic result (solid lines). The high opacity test results are shown in the left panel and the low opacity test results are shown in the right panel. We show the energy density ( $E$ ), flux factor ( $f = F_r/E$ ), and the Edington factor ( $p = p_{rr}/E$ ). These tests are Newtonian—there are no general relativistic or velocity effects. Our transport scheme does well in both the optically thick (with both high and low Peclet number) region and in the free streaming region. The results of this test are particularly sensitive to the closure relation. For our results we use the Minerbo closure. Smit et al. (1997) found significant variation of their results with the choice of closure. The variation is of order what we see in Fig. 1. The optimal choice of closure is an outstanding question, but will not be addressed here.

Since we use an evenly-spaced grid, and all of the zones outside of the sphere are free streaming, the first-order explicit flux calculation with a Courant factor of 0.5 gives artifacts in the radiation moments exterior to the sphere. For this test we avoid this by evolving the spatial flux in low Peclet number cells ( $\text{Pe} < 0.01$ ) via the second-order explicit midpoint method. The ultimate solution is the implementation of higher order implicit-explicit methods valid in the optically thick regime. This is beyond the current work, but as noted in §2.5, in typical CCSN conditions and with the grid we use in GR1D we typically do not numerical problems when using the first-order explicit method.

##### 4.2. General Relativistic Radiating Sphere with Velocity Field

To test the energy coupling terms discussed in §2.4 we repeat the tests performed in Müller et al. (2010). These tests use a gravitating radiating sphere as a source of a spectrum of neutrinos which radiate through a velocity field similar to what is found in CCSNe. For the radiation, we choose a thermal Fermi spectrum with a temperature of 5 MeV and zero chemical potential. We use our standard energy group spacing. We logarithmically space 18 groups with the first group centered at 1 MeV with a width of 2 MeV. The largest bin is centered at  $\sim 280.5$  MeV with a width of  $\sim 61$  MeV. Our spatial grid is also logarithmic with a central zone spacing of  $10^4$  cm, extending to a radius of  $10^9$  cm over 300 zones. The spatial zone spacing at the velocity feature is the same as Müller et al. (2010),  $\sim 4$  km. We make the absorption opacity in the interior of the radiating sphere sufficiently high such that, to a good approximation, all of the escaping radiation comes from the surface (like the first radiating sphere test case above). A velocity profile similar to what is found in the stalled shock phase of CCSNe is also used. These two features test both the  $R_\alpha$  (gravitating) and  $O_\alpha$  (accelerating) momentum flux terms. We test three cases: *a*) a 9.89 km radi-

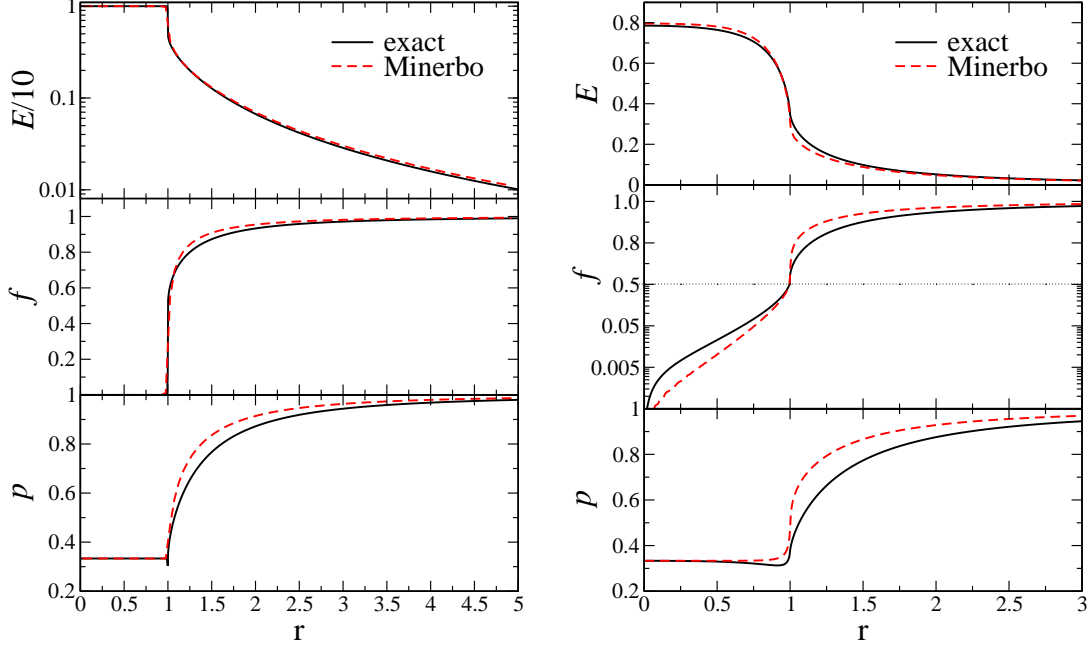


**Figure 1.** Classical radiating spheres with two different neutrino interaction rates for the interior of the sphere. In the left panel we repeat the test of Abdikamalov et al. (2012) which is a highly opaque sphere with an optical depth at the center of 250. In the right panel we repeat the test of Smit et al. (1997) that models a sphere with a much lower opacity, here the optical depth in the center is 4. In both panels we show, from the top down, the energy density ( $E$ ), the flux factor ( $f = F_r/E$ ), and the Eddington factor ( $p = p_r/E$ ). The solid black line denotes the exact solution while the dashed red line is our numerical result using the Minerbo closure. We note the vertical axis in the right-middle panel transitions at the dotted line from linear for  $f > 0.5$  to logarithmic for  $f < 0.5$ , this is to clearly show the behavior in both regimes.

ating sphere of negligible mass with the velocity profile used in Müller et al. (2010), *b*) a 9.89 km radiating sphere of dust with a constant density of  $9 \times 10^{14} \text{ g cm}^{-3}$  such that the gravitating mass is  $\sim 1.833 M_\odot$  but no velocity field, *c*) both the gravitating radiating sphere and the velocity profile used in the previous cases.

The velocity profile is taken from Müller et al. (2010),

$$v(r) = \begin{cases} 0; & r \leq 135 \text{ km} \\ -0.2c \frac{r-135 \text{ km}}{15 \text{ km}}; & 135 \text{ km} < r < 150 \text{ km} \\ -0.2c \left(\frac{150 \text{ km}}{r}\right)^2; & r \geq 150 \text{ km} \end{cases} \quad (64)$$

We will first discuss the analytic solutions which also follow closely to those in Müller et al. (2010). For the luminosity, the analytic expression can be determined by taking the free streaming limit of the fluid frame flux (Eq. 54 with  $E = F_r/X = P_{rr}/X^2$ ) and noting that the energy integrated, static solution of Eq. 9, in the vacuum limit, gives  $\alpha r^2 \int_\epsilon F_r d\epsilon / X^2 = \text{const}$ , where  $\int_\epsilon d\epsilon$  denotes the integral over the energy spectrum. Therefore,

$$\mathcal{L}(r) = (4\pi r)^2 \int_\epsilon \mathcal{H}^r d\epsilon = (4\pi)^2 \frac{W}{\alpha} \frac{1-v}{1+v} \frac{\alpha r^2 \int_\epsilon F_r d\epsilon}{X^2}. \quad (65)$$

It follows from this that in the free streaming limit, variations in the fluid frame luminosity should arise only due to non-zero velocities and gravitational redshift,

$$\mathcal{L}(r) \propto \frac{W}{\alpha} \frac{1-v}{1+v}. \quad (66)$$

The standard relativistic Doppler effect applies for the average energy as measured in the fluid frame with the general

relativistic addition here to account for the gravitational redshift as the neutrinos stream away from the source,

$$\langle \epsilon \rangle(r) = \frac{\alpha(r_{\text{surface}})}{\alpha(r)} \frac{\langle \epsilon_{\text{surface}} \rangle}{W(1+v)} \sim \frac{\alpha(r_{\text{surface}})}{\alpha(r)} \frac{15.7568 \text{ MeV}}{W(1+v)}, \quad (67)$$

where the 15.7568 MeV is the average neutrino energy of a Fermi distribution with zero chemical potential and a temperature of 5 MeV. The analytic solution motivates the high opacity mentioned above so that all of the radiation that reaches infinity was originally emitted from  $r = r_{\text{surface}}$  and not from deeper in where the appropriate redshift correction factor would be different than  $\alpha(r_{\text{surface}})$ . For reference,  $\alpha(r_{\text{surface}}) = 0.6723$ .

In Fig. 2 we show the fluid frame neutrino luminosity and average energy as a function of radius from GR1D for each of these three tests. We also show analytic solutions as solid lines. For the luminosities, we normalize the solution to the simulation value at  $r = 10^4 \text{ km}$  and then scale every solution by  $\alpha_{\text{surface}}^2$ . For the gravitating spheres, in addition to the redshift effect, the luminosity is suppressed by an additional factor of  $\alpha_{\text{surface}}$  due to general relativistic time dilation at the source. For the average energy analytic solution, we use Eq. 67 directly and do not normalize the data in any way. The data from GR1D are shown as the blue dashed lines (case #1), green dotted lines (case #2), and red dotted-dashed lines (case #3). Additionally, we show the relative difference between the analytic solution and our data. The observed deviations are  $< 1\%$  for both the luminosity and the average energy. The effect of the first order explicit flux calculation can be seen for small radii. To be clear, since we evolve the lab frame variables  $E$  and  $F_r$  and compute the fluid frame value shown here with Eq. 54 and the closure, this test shows that the total luminosity in the lab frame is constant as a function of radius (to better

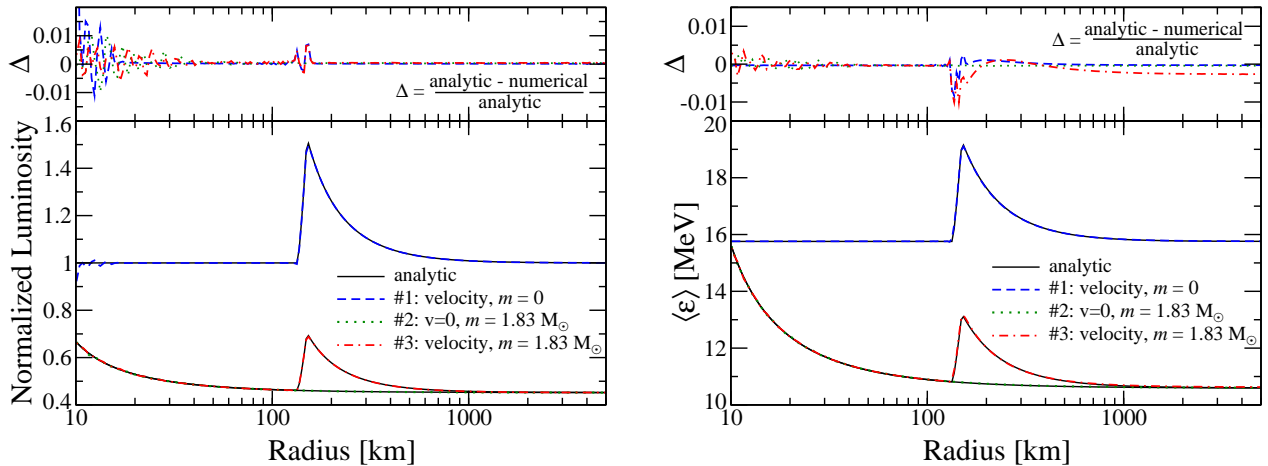


**Figure 2.** Gravitating radiating spheres with a velocity field based on the test cases of Müller et al. (2010). We conduct three separate radiating sphere simulations: the first sphere (#1) has a negligible mass but has the velocity profile of Eq. 64, the second test (#2) has no velocity field, but the sphere has a gravitational mass of  $1.833 M_{\odot}$ , the third case (#3) is both gravitating and contains the velocity profile of Eq. 64. In the left figure we show the fluid frame luminosity, normalized to the sphere’s value at infinity. We also apply the expected factor of  $\alpha_{\text{surface}}^2 \sim 0.452$  to this normalization. In the right figure we show the fluid frame average energy. For both figures we include the analytic prediction, and also the relative deviation ( $\Delta$ ) of our simulations from these analytic predictions.

than 1% at  $r = 150$  km), as expected. However, even though the total luminosity in the lab frame is constant, this does not mean the distribution of the energy among the energy groups remains constant. Recall that our definition of neutrino energy applies only in the fluid rest frame, therefore when fluid velocities exist, even if the neutrinos are completely decoupled from the fluid ( $\eta = \kappa_a = \kappa_s = 0$ ) the energy of a particular energy group in the lab frame is not the same as the fluid frame. When the fluid velocity is changing (either in time or radially), this induces a flux between neighboring energy groups which is captured in  $O_{\alpha}$ .

These tests provide a clean environment to test for neutrino number and energy conservation in our code. By tracking the energy and neutrino number emitted/absorbed by the matter in the radiating sphere plus the energy and neutrino number exiting the outer boundary and computing the energy and neutrino number present on the grid we can track violations. For test case #1, #2, and #3, the neutrino number violation is  $\sim 0.5\%$ ,  $\sim 2\%$ , and  $\sim 2\%$  respectively while the energy conservation is  $\sim 0.5\%$ ,  $\sim 0.03\%$ , and  $\sim 0.07\%$ , respectively. For a test case with neither velocity nor a gravitating mass, the number violation and energy violation is  $\sim 0.01\%$ . The majority of the lepton violation in the gravitating sphere cases (#2 and #3) occurs in the sphere itself rather than the free streaming region outside.

#### 4.3. Diffusion Wave

The final basic code test we perform is a diffusion wave test. This test is identical to the diffusion test of Pons et al. (2000). The purpose of this test is to show the ability of our explicit flux implementation to perform in very diffusive conditions that would normally fail without the corrections made in §2.5. The test problem is to follow the diffusion of a Dirac delta function of radiation located at the origin at  $t = 0$ . In the diffusion limit the analytic solution is,

$$E = \left(\frac{\kappa}{t}\right)^{3/2} \exp\left(\frac{-3\kappa r^2}{4t}\right); \quad F_r = \frac{r}{2t}E. \quad (68)$$

Following Pons et al. (2000), we take a spherical grid extending to a radius of 1 using 100 equally spaced zones. We do two

tests on this grid. Test A takes a scattering opacity  $\kappa_s = 100$  (giving a  $Pe = 1$ ) and starts the simulation from  $t = 1$  to avoid the delta function at  $t = 0$ . Test B takes a scattering opacity of  $\kappa_s = 10^5$  ( $Pe = 1000$ ) and starts the simulation at  $t = 200$ . We sample our simulations at three additional times,  $t = 2, 3$ , and 5 for test A and  $t = 240, 300$ , and 400 for test B. Unlike Pons et al. (2000) we use our standard closure shown in Eq. 21 rather than taking  $p_{rr} = 1/3$ , however, we find such a choice makes little difference since the momentum density is always much less than the energy density.

In Fig. 3 we show our results compared to the analytic solution. In the left two panels are the results of test A with the energy density on the left and momentum density on the right. In the right two panels are the results of test B, again with energy density on the left and momentum density on the right. We note the first result in both cases ( $t = 1$  and  $t = 200$  in test A and B, respectively) is the initial setup, and therefore the GR1D result is identical to the analytic result. GR1D can reproduce the diffusion limit analytic solution quite well. For test B, we do find differences that we can explain in part from our interpolation choice between the diffusion limit and hyperbolic limit of the flux determination (i.e. the value of  $a$  in Eq. 44 and Eq. 45). If we assume  $a = 0$  in order to force the spatial flux calculation to be determined by the diffusion approximation we can achieve a result closer to the analytic solution than what is shown in Fig. 3. We are not worried about the differences seen here significantly affecting our CCSN simulations for several reasons. First, a Peclet number of 1000 is quite large. In CCSN simulations we only reach these values for the largest energy groups ( $\sim > 150$  MeV) in high density zones. Also, the simulation times we consider are much less than the diffusion time of the neutrinos in regions with these high Peclet numbers. For applications of this code to proton-neutron star cooling it will be necessary to further explore this regime.

## 5. CORE-COLLAPSE SUPERNOVAE TEST PROBLEMS

### 5.1. Comparison with other Neutrino Transport Codes

A somewhat standardized test of spherically symmetric, general relativistic, neutrino radiation hydrodynamics is the

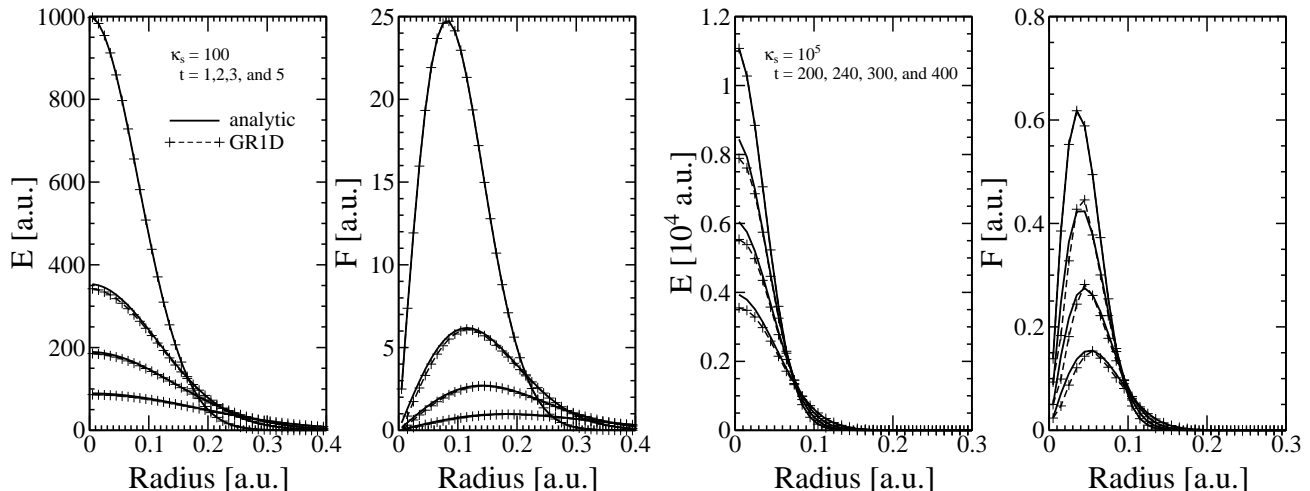


**Figure 3.** Diffusion of a centralized packet of radiation. In the left two panels are the results of a test where the grid spacing and opacity give a Pecllet number of 1. The simulations depicted in the right two panels however use a much larger opacity and the Pecllet number is 1000. The left panel of each simulation shows the energy density, the right panel shows the momentum density. As time progresses and the radiation diffuses out, the curves decrease in magnitude. The tests are identical to those in Pons et al. (2000).

collapse, bounce, and early post-bounce evolution of the  $15M_{\odot}$  progenitor star of Woosley & Weaver (1995) using the EOS from Lattimer & Swesty (1991) with  $K_0 = 180\text{MeV}$  (LS180) and a set of simplified neutrino rates from Bruenn (1985). The LS180 EOS has a maximum cold neutron star gravitational mass of  $1.84M_{\odot}$ . This maximum mass has been ruled out by the observation of  $\sim 2M_{\odot}$  neutron stars (Demorest et al. 2010; Antoniadis et al. 2013), however, it has been used in several other studies as a basis for comparison (Liebendörfer et al. 2005; Müller et al. 2010). For this reason alone, we also use it here. The simulation data of Liebendörfer et al. (2005) are publicly available via the publisher’s website. We use that data here to show GR1D’s ability to simulate the core collapse, bounce, and post-bounce phases of a CCSN in spherical symmetry. It is worth mentioning that the weak magnetism and recoil corrections of Horowitz (2002) are not included in the work of Liebendörfer et al. (2005), and therefore are also not included in this comparison. The comparison data in Liebendörfer et al. (2005) is between two simulation codes, *Agile-BOLTZTRAN* and *VERTEX*. *Agile-BOLTZTRAN* is a fully general relativistic, Lagrangian hydrodynamics code with a Boltzmann neutrino transport solver while *VERTEX* is a Newtonian, Eulerian hydrodynamics code with a gravitational potential correction to mimic the effects of general relativity. *VERTEX*’s transport is a moment scheme with a variable Eddington factor solved via a model Boltzmann equation. Improvements to *VERTEX* after Liebendörfer et al. (2005), and other comparisons (Marek et al. 2006; Müller et al. 2010), suggest that the publicly available data in Liebendörfer et al. (2005) from *Agile-BOLTZTRAN* are more reliable than those from *VERTEX*.

Our simulation uses the following energy grid for each neutrino type, we logarithmically space 18 groups with the first group centered at 1 MeV with a width of 2 MeV. The largest bin is centered at  $\sim 280.5\text{MeV}$  with a width of  $\sim 61\text{MeV}$ . We assume three neutrino species by lumping  $\nu_{\mu}$ ,  $\bar{\nu}_{\mu}$ ,  $\nu_{\tau}$ , and  $\bar{\nu}_{\tau}$  into a characteristic heavy-lepton neutrino  $\nu_x$ . The spatial grid is a hybrid grid where the inner 20 km is evenly spaced with 100 zones of 200 m each. Outside of this radius we use a logarithmically spaced grid consisting of 550 zones from 200 km out to  $\sim 15000\text{km}$ . To be clear, for the following comparison

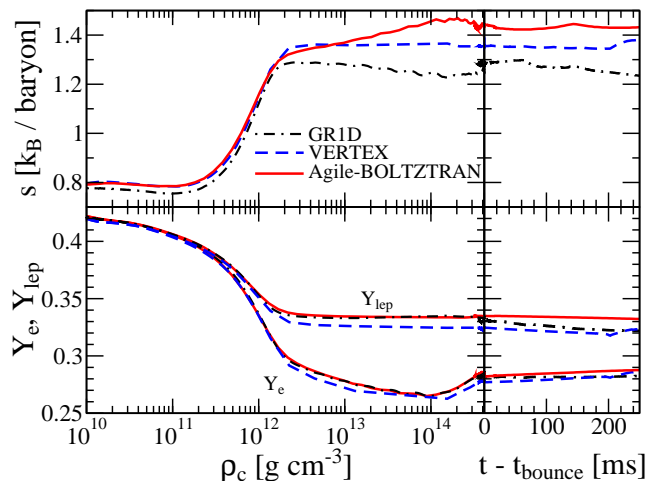


**Figure 4.** Evolution of central entropy and lepton numbers. In the left (right) panels are the pre-bounce (post-bounce) values of the central entropy [top] and electron ( $Y_e$ ) and total lepton ( $Y_{\text{lep}} = Y_e + Y_{\nu}$ ) fraction [bottom]. Pre-bounce we show these values versus the central density, while after bounce we show them versus time. GR1D’s values are the black dashed-dotted lines, AGILE results are shown as red solid lines and the VERTEX results are shown as blue dashed line.

simulation we use an explicit treatment of inelastic neutrino-electron scattering and the pair-production approximation discussed in §2.6.2 and §3. We explore these approximations in the following section.

In Fig. 4, we show the evolution of the central entropy (top panels) and the electron ( $Y_e$ ) and total lepton number ( $Y_{\text{lep}} = Y_e + Y_{\nu}$ ) fractions (bottom panels) along with the *Agile-BOLTZTRAN* and *VERTEX* results from Liebendörfer et al. (2005). To more clearly show the evolutionary changes we split the simulation into the pre-bounce phase (left) and post-bounce phase (right). Most of the interesting neutrino physics happens in the final  $\sim 10\text{-}20\text{ms}$  of the collapse phase as the central density rises from  $\sim 10^{11}\text{g cm}^{-3}$  to  $\sim 10^{14}\text{g cm}^{-3}$ , therefore we show this phase versus central density. After bounce we plot the quantities versus post-bounce time as the central density during this time is essentially constant. We first discuss the lepton fraction. The agreement between the GR1D and the Boltzmann solutions, particularly with *Agile-*

BOLTZTRAN, during the collapse phase is exceptional and relies heavily on the implementation of inelastic neutrino-electron scattering, energy bin coupling, and neutrino advection with the fluid in the optically thick medium. However, we note that Lentz et al. (2012) have shown that improved electron capture rates on heavy nuclei beyond what was used in Liebendörfer et al. (2005) can play the role that inelastic neutrino-electron scattering plays here. There are small oscillations in both the neutrino and electron fraction between densities around  $10^{13} \text{ g cm}^{-3}$  and nuclear density that are the result of equilibration between the electrons and neutrinos as the electron chemical potential of the matter rises and the discretely spaced neutrino energy levels fill up. This is present in both the *Agile*-BOLTZTRAN results and ours and can be eliminated with increased energy resolution as has been shown by Rampp & Janka (2002). The VERTEX data from Liebendörfer et al. (2005) has too low of temporal resolution to see this effect. The total lepton fraction is essentially constant after the electron neutrinos become fully trapped, which occurs in the core, around  $\rho \sim 2 \times 10^{12} \text{ g cm}^{-3}$ . For the post-bounce evolution, over the simulated 250 ms, the central lepton and electron fractions remain roughly constant with some secular drift. We find that the central neutrino fraction drops similarly in all three codes, but that GR1D's central electron fraction does not increase as is seen in the Boltzmann codes, but rather remains constant.

In the top panel of Fig. 4 we show the evolution of the matter entropy in the innermost zone. We again show the pre-bounce evolution versus central density on the left and the post-bounce evolution versus time on the right. The different starting values of the entropy between the codes is likely due to the different implementations of the nuclear EOS. Aside from this shift, the evolution is similar. Before trapping, the entropy rises due to neutrino interactions, but after the onset of neutrino trapping the matter entropy should remain constant, we see an initially lower value and then a small decrease as the matter density increases to nuclear densities. We note that the entropy shown here is only the matter entropy, it does not include the entropy of the neutrinos, which is small and roughly constant throughout the trapping region. After bounce the entropy remains roughly constant, but decreases by about 4% over the 250 ms. While concerning, and clearly an area for future improvement, these aspects of the central core evolution do not have a large impact on the rest of the protoneutron star within the first few 100 ms or even up to a second after core bounce since the neutrino diffusion time is long compared to the times simulated here.

In Fig. 5 we show a collection of profiles showing the results of both GR1D and *Agile*-BOLTZTRAN. The VERTEX results, after improving the pseudo-relativistic potential in Marek et al. (2006), agree very well with the *Agile*-BOLTZTRAN results. We include profiles of the neutrino luminosity (left panels), neutrino root mean squared energy (center panels), and electron fraction and entropy (right panels). The luminosity follows from the first expression in Eq. 65 and the root mean squared energy is computed by averaging  $\epsilon^2$  over the fluid frame neutrino number distribution, equivalent to the definition in Liebendörfer et al. (2005). We show these profiles at bounce (top panels), 3 ms after bounce (middle panels), and 100 ms after bounce (bottom panels). For the heavy lepton neutrino luminosity, we average the neutrino and antineutrino results from *Agile*-BOLTZTRAN. GR1D agrees very well with the *Agile*-BOLTZTRAN results in almost

every quantity.

At bounce, defined as when the entropy in the core region first reaches a value of  $3 k_B/\text{baryon}$ , the electron antineutrino production is still highly suppressed from the high electron chemical potential, its luminosity is off the bottom of the panel. The other neutrino luminosities have a strong peak in production at  $\sim 10 \text{ km}$  which corresponds to the shock formation radius. We note that the baryonic mass enclosed in the shock at this time is  $\sim 0.54 M_\odot$  in *Agile*-BOLTZTRAN and  $\sim 0.55 M_\odot$  in GR1D. There are some artifacts in the root mean squared energy of the electron antineutrino profile at this time, but the reader is reminded that the total energy in these neutrinos is very small. The entropy and electron fraction profiles agree very well at this time. There is a slight difference in the  $Y_e$  of the accreting material, but it is important to note that this is a very dynamic time. For example, a GR1D profile from a mere  $50 \mu\text{s}$  earlier reproduces the  $Y_e$  profile in the accretion region (outside the shocked core) of the *Agile*-BOLTZTRAN profile.

At 3 ms after bounce, all of the quantities plotted in the middle panels of Fig. 5 show exceptional agreement between GR1D and *Agile*-BOLTZTRAN. GR1D reproduces every divot, bump, peak, and trough in the luminosity, root mean squared energy, entropy and electron fraction. The largest discrepancy is the electron antineutrino root mean squared energy in the core. However, there is very little total electron antineutrino energy density in the core, so this is not a large concern. The likely culprit is our lack of pair production processes (and nucleon-nucleon Bremsstrahlung in particular which dominates the rate in the unshocked, dense core) in the electron neutrino/antineutrino sector. A similar electron antineutrino root mean squared energy was seen in the Newtonian results of Liebendörfer et al. (2005) where nucleon-nucleon Bremsstrahlung was omitted. However, even if this was included, the extreme electron degeneracy in the core keeps the energy density of electron antineutrinos orders of magnitude lower than that of the electron neutrinos.

At 100 ms after bounce, the bottom panels of Fig. 5 show that inside of  $\sim 100 \text{ km}$ , we continue to see excellent agreement. In the inner 20-25 km, the luminosity in all three flavors matches between the codes, including the inward diffusion of the electron antineutrino and the heavy-lepton flavor neutrinos near the location of shock formation and the boundary between the shocked and unshocked core. The electron neutrino and antineutrino luminosities and energies agree well between the codes, including the location and strength of the gain regions, out to  $\sim 130 \text{ km}$ , where we reach the shock front in GR1D. This is the single biggest difference between our simulations and those of Liebendörfer et al. (2005); Marek et al. (2006); Müller et al. (2010). We discuss this in the following section when we look at the time evolution of the neutrino observables. The heavy-lepton neutrino luminosity and root mean squared energy deviates from the *Agile*-BOLTZTRAN near its neutrinosphere. Considering the simplicity of our approximation for the heavy-lepton neutrino production/annihilation we achieve remarkable agreement. We explore this in much greater detail in the following section where we assess our approximations. At the shock front, since we are showing the fluid frame neutrino quantities, the luminosity and root mean squared energy jump. Due to GR1D's hydrodynamics, the shock is better resolved, resulting in a sharper (and larger) jump in the fluid frame luminosity.

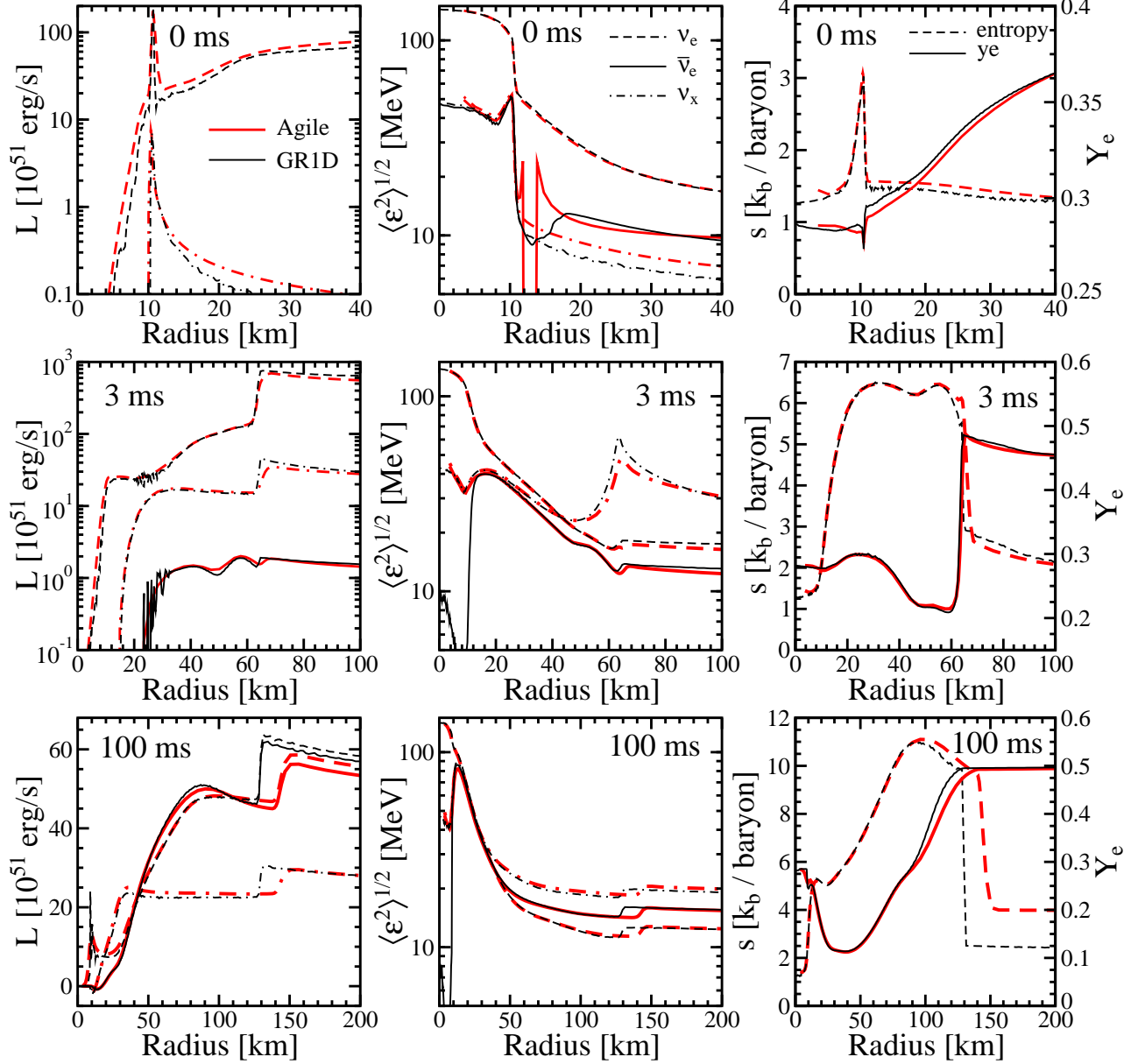


**Figure 5.** Comparison of radial profiles. We show various radial profiles from GR1D (thinner black lines) and *Agile*-BOLTZTRAN (thicker red lines) at three times: bounce (top panels), 3 ms after bounce (middle panels), and 100 ms after bounce (bottom panels). At each time we show each neutrino flavor’s luminosity (left panels), root mean squared energy (center panels), and profiles of the entropy and electron fraction (right panels). For the neutrino quantities, the profiles for electron neutrinos use a dashed line, electron antineutrinos are shown with a solid line, and the heavy-lepton neutrino profiles are shown with a dashed-dotted line. The entropy profiles use a dashed line while the electron fraction profile lines are solid. Overall, the agreement between GR1D and *Agile*-BOLTZTRAN is excellent.

ties and energies. Outside of the shock, *Agile*-BOLTZTRAN burns silicon to nuclear statistical equilibrium (NSE) when the temperature surpasses 0.44 MeV, whereas in GR1D we incorrectly, but for simplicity, assume NSE everywhere. This results in differences in the entropy outside of the shock.

As another comparison, we look at the far-field neutrino luminosities and root mean squared energies versus time for the first 250 ms after bounce. Following the convention of Liebendörfer et al. (2005), we show these quantities in the fluid frame at 500 km. However, we note that the velocity at this radius can be  $\sim 0.06c$  and therefore these energies and luminosities are roughly 6% and 12% larger, respectively, than one would observe at Earth. We compare our results to

those obtained with both VERTEX<sup>7</sup> and *Agile*-BOLTZTRAN. In GR1D, by default, we do not include electron antineutrinos or heavy-lepton neutrinos before the central density reaches  $10^{12} \text{ g cm}^{-3}$  as they have very little luminosity and no dynamical effect on the simulation. We show these comparisons in Fig. 6. This plot is very similar to the version we presented in O’Connor & Ott (2013), however, our transport code has been significantly improved since then. The average energies

<sup>7</sup> Improvements made to the VERTEX code after the publication of Liebendörfer et al. (2005) change the predicted neutrino luminosities (Marek et al. 2006). These changes lead to lower luminosities that have magnitudes similar to the *Agile*-BOLTZTRAN results. However, and this is relevant to our results, the sharp drop in the neutrino luminosity around  $\sim 180$  ms remains.

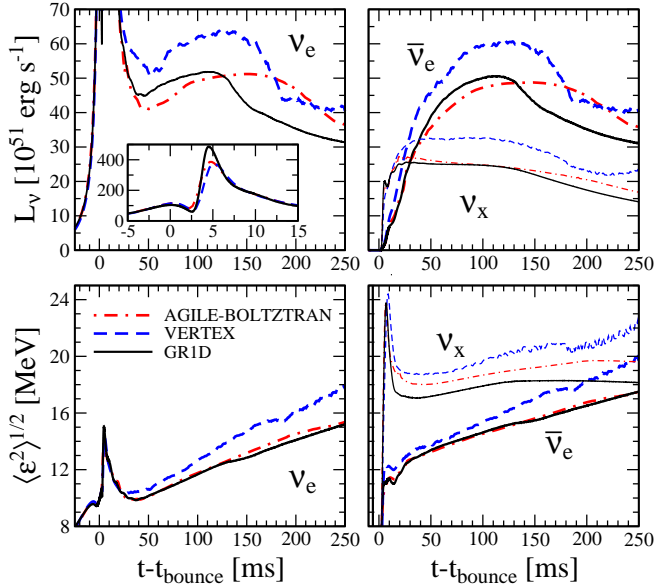


**Figure 6.** Comparison of time evolutions of key neutrino quantities. We show the time evolution of the neutrino luminosity (top panels) and the neutrino root mean squared energy (bottom panels) as measured by an observer moving with the fluid at 500 km. Results of GR1D are shown as solid black lines, *Agile*-BOLTZTRAN results are shown as dashed-dotted red lines, and VERTEX results are shown as dashed blue lines. The left two panels are the luminosity and root mean squared energy of electron neutrinos, the right two panels show this information for both electron antineutrinos (thick lines) and the heavy-lepton neutrino (thin lines). The inset in the upper left panel show just the deleptonization burst near the time of bounce.

from GR1D over the entire 250 ms are in excellent agreement with the *Agile*-BOLTZTRAN results. The largest difference is in the heavy-lepton neutrino root mean squared energy that we under-predict by  $\sim 1$  MeV. ( $\sim 6\%$ ) compared to the *Agile*-BOLTZTRAN simulation. We comment on this further in §5.2.

The luminosities between GR1D and *Agile*-BOLTZTRAN up to  $\sim 100$  ms are in general agreement. We note that the luminosities of Müller et al. (2010) are also generally higher than those of *Agile*-BOLTZTRAN in the first 100-150 ms, and also during the deleptonization peak. This may be due to the higher resolution at the shock front that we discussed in the context of the radial luminosity profiles above, an effect which is also seen in the simulations of Müller et al. (2010). The heavy-lepton neutrino luminosity follows the *Agile*-BOLTZTRAN results very closely. We discuss this agreement more in the context of exploring the approximation we make for the pair-production processes in the following section (§5.2). At  $\sim 130$  ms, the silicon-oxygen interface accretes through the shock and causes a drop in the neutrino luminosities. A similar effect is seen in the VERTEX data, although at a later time. The adaptive grid of *Agile*-BOLTZTRAN smears out the jump in density at the interface and such a steep drop in neutrino luminosities is not seen. It is currently unknown why the silicon-oxygen interface accretes through the shock earlier in GR1D when compared to VERTEX. However, the difference in the collapse times ( $\sim 225$  ms in GR1D compared to  $\sim 170$  ms in VERTEX and *Agile*-BOLTZTRAN) is suggestive that the problem is rooted in the low density EOS which as mentioned above, does not include any burning or non-NSE physics. This problem is particularly difficult to diagnose since core collapse is a critical phenomenon. Investigations are ongoing.

A crucial role of neutrinos in CCSNe is to deposit energy in

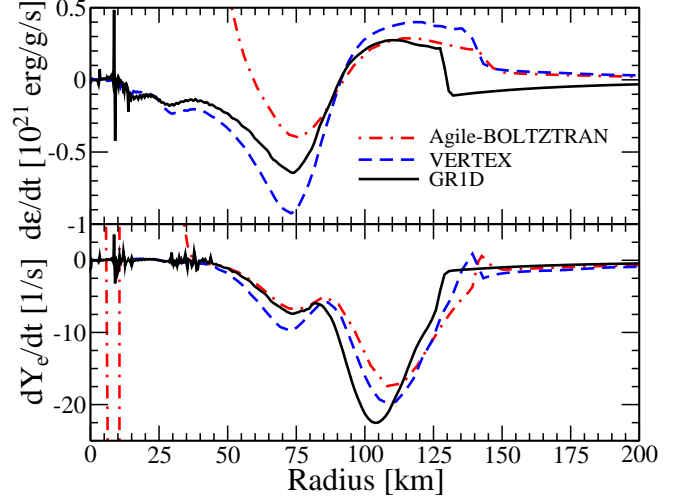


**Figure 7.** Rates of change of specific internal energy (top panel) and lepton number (bottom panel) versus radius at a postbounce time of 100 ms. In addition to the GR1D results shown as black solid lines, we show the results from Liebendörfer et al. (2005). Red dashed-dotted lines are the *Agile*-BOLTZTRAN data, while the blue dashed lines are the VERTEX results.

the outer layers of the postshock region. This deposition leads to the generation of the so-called gain region, where there is a net positive exchange of energy from the radiation field to the matter. The efficiency of energy absorption in the gain region is small ( $\lesssim 10\%$ ), but it is likely a very important aspect of supernova shock revival. We look at several quantities to ensure that our transport scheme is adequately capturing the effects of neutrino heating. In Fig. 7, we show the rate of energy (top) and lepton (bottom) exchange from the neutrinos to the matter as a function of radius, at 100 ms after bounce<sup>8</sup>. As in the other figures, we show the *Agile*-BOLTZTRAN and VERTEX results as red dashed-dotted and blue dashed lines, respectively. In all three simulations, interior to the gain region (where  $d\epsilon/dt > 0$ ) all simulations show a significant cooling region. As mentioned above, the VERTEX simulation over-predicts the neutrino luminosity which is a result of the higher cooling rate seen here. *Agile*-BOLTZTRAN's  $d\epsilon/dt$  in the public data suffers from a bookkeeping error which results in the energy and lepton exchange rates being calculated for output when the electron neutrino and electron antineutrino are slightly out of equilibrium (Liebendörfer 2015). This makes a comparison at small radii (and even into the cooling region) difficult. In all codes, the gain region begins at  $\sim 90$  km and extends out to the shock (which is  $\sim 15$ - $20$  km lower in GR1D). Outside of the shock GR1D returns to a net cooling, while the other simulations continue to show net heating. This is likely due to the thermodynamic conditions outside of the shock. In the Boltzmann transport codes the entropy is much higher outside the shock from a more complete treatment of the low density, non-NSE material. This gives a higher abundance of free neutrons, which increases the opacity for antineutrino capture in this region. The lepton exchange rates from GR1D also track the full Boltzmann results fairly well. The main differences are near the shock and originate from the different shock locations.

As a final comparison, in Fig. 8, we show the shock evo-

<sup>8</sup> In practice, we change the conservative hydrodynamic quantities which are non-linear combinations of  $\rho$ ,  $P(\epsilon)$ ,  $Y_e$ , and  $v$ . For this figure, we approximate  $dY_e/dt$  as Eq. 60 divided by  $D\Delta t$  (the  $D = \rho W X$  quantity is conserved over the radiation time step). We show  $d\epsilon/dt$  as Eq. 58 divided by  $\rho\Delta t$ .

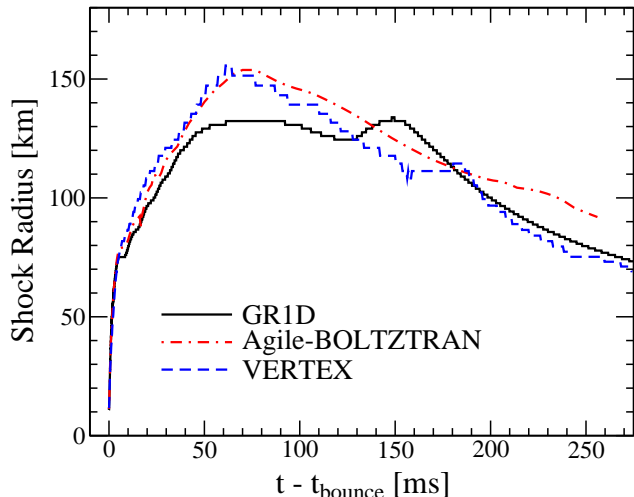


**Figure 8.** Shock radius evolution over time. In addition to the GR1D results shown as black solid lines, we show the results from Liebendörfer et al. (2005). Red dashed-dotted lines are the *Agile*-BOLTZTRAN data, while the blue dashed lines are the VERTEX results.

lution in GR1D, *Agile*-BOLTZTRAN, and VERTEX. The most significant difference is the extent to which the shock reaches before it ultimately starts to recede, GR1D under-predicts this by  $\sim 20$  km. As was apparent in the electron type neutrino luminosity evolution, the time of the silicon-oxygen interface accretion through the shock can also be seen in the shock radius evolution in both GR1D and VERTEX. The accretion of this interface results in a brief period of shock expansion as the accretion rate drops quickly. This occurs later in the VERTEX simulation.

## 5.2. Validity of Transport Approximations

To test the validity of our heavy-lepton neutrino approximation we perform two additional simulations. First we carry out a collapse simulation of the  $15-M_{\odot}$  model without our approximation but using instead a kernel-based treatment of  $e^+ + e^- \leftrightarrow \nu_x + \bar{\nu}_x$ . We compare it to a simulation using our approximate method. As a reminder, our approximation is to assign an emissivity ( $\eta^{pp}$ ) assuming no final state neutrino blocking and use an effective absorption cross section computed via  $\kappa_a^{pp} = \eta^{pp}/B_{\nu}$ , where  $B_{\nu}$  is the value of the black body function for that energy. This removes coupling between energy groups and species. In both cases we only implement these rates for heavy-lepton neutrinos. For a one-to-one comparison, these simulations we omit nucleon-nucleon Bremsstrahlung since NuLib does not have kernels for this process.

In Fig. 9, we show the results of these two simulations (the solid line for the kernel-based treatment and the dashed line for the approximation). For clarity, we only show the heavy-lepton neutrino luminosities (top panel) and root mean squared energies (bottom panel). The electron-type neutrino quantities are not directly influenced by this treatment and change very little. In addition, we include the *Agile*-BOLTZTRAN results (dashed-dotted-dotted line) for comparison. Our approximation results in a  $\sim 7\%$  lower value of the luminosity for the first  $\sim 150$  ms. Coincidentally, this  $\sim 7\%$  difference is also the difference one expects for excluding nucleon-nucleon Bremsstrahlung. The latter was noted in Lentz et al. (2012), but we can also see the effect in our simulations. Also shown in Fig. 9 (as the dashed-dotted-dotted line) is

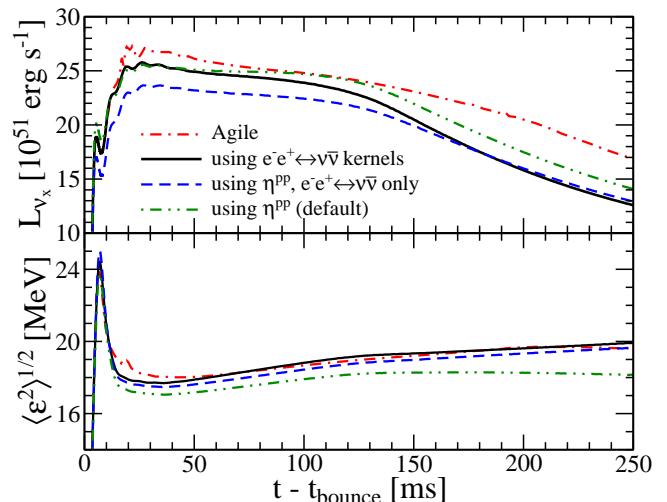


**Figure 9.** Investigating the pair production approximations in GR1D. We show the emitted heavy-lepton luminosity (top panel) and root mean squared energy (bottom panel) for several simulations designed to study the effect of our approximations. Our standard simulation is shown as the green dashed-dotted-dotted line and corresponds to the results in Fig. 6. We also show results from GR1D using this approximation but only including  $e^- + e^+ \leftrightarrow \nu_x + \bar{\nu}_x$  as the blue dashed line and the results of an implicit approach with production and annihilation kernels for  $e^- + e^+ \leftrightarrow \nu_x + \bar{\nu}_x$  as the solid black line. For reference we show the *Agile*-BOLTZTRAN results as a thick red dashed-dotted line. There is very little influence on the electron neutrino and antineutrino luminosities and root mean squared energies between these simulations.

the reference simulation from the previous section that uses our heavy-lepton approximation but includes both electron-positron annihilation and nucleon-nucleon Bremsstrahlung as sources. The difference between this line and the dashed line is the effect of nucleon-nucleon Bremsstrahlung. These two results together explain the similarity of the kernel-based luminosity and the approximation seen in Fig. 9 and predict that a full kernel-based treatment would see a luminosity that is roughly  $\sim 7\%$  higher than the kernel-based treatment with only electron-positron annihilation. Such a luminosity would be in better agreement with the results of Liebendörfer et al. (2005) and Müller et al. (2010).

The heavy-lepton root mean squared energies (bottom panel of Fig. 9) are also well captured by our pair production approximation. When comparing the proper kernel treatment to the equivalent simulation that uses the approximation (solid line to the dashed line), our approximation gives a slightly ( $\sim 2\%$ , or  $0.3$  MeV) lower root mean squared energy consistently throughout the first 250 ms of post-bounce evolution. All of these variations in the root mean squared energy are within the error bounds set by other simulation codes (c.f. Liebendörfer et al. 2005; Marek et al. 2006; Müller et al. 2010). Inclusion of nucleon-nucleon Bremsstrahlung in our approximate method (dashed-dotted-dotted line in the bottom panel of Fig. 9) reduces the root mean squared energy by a further  $\sim 1$  MeV.

The second approximation is our explicit treatment of inelastic neutrino-electron scattering. The results above treat neutrino-electron scattering explicitly throughout the entire evolution. As mentioned in §2.6.2, we place a suppression on the high density ( $\rho > 5 \times 10^{12}$  g cm $^{-3}$ ) scattering kernels to enable our explicit treatment. This kernel suppression is necessary to keep the scattering amplitudes small and is the main source of error, rather than any explicit versus implicit implementation differences. To test this, we perform a sim-

ulation where we treat inelastic neutrino-electron scattering implicitly. We see essentially no differences in the hydrodynamic quantities and the electron neutrino and antineutrino luminosities and root mean squared energies. The largest differences arise in the heavy-lepton sector, as expected, since these neutrinos are being emitted from the highest density regions where our artificial reduction of the kernels is being implemented. To fully see the effect of this approximation, we test our explicit/implicit inelastic neutrino-electron scattering approximation using an implicit treatment of heavy-lepton neutrino production. The observed differences in the heavy-lepton neutrino luminosities and root mean squared energies reach the 2% level around 200 ms. As the heavy-lepton neutrinosphere recedes to higher densities this difference increases. Our suppression of the scattering kernels at high density reduces the efficiency of down-scattering neutrinos and the emitted spectrum has a larger root mean squared energy and a lower overall neutrino luminosity.

### 5.3. Neutrino Number Conservation

We test neutrino number conservation via a simplified scenario described here. We take several configurations from the standard run in §5.1 and evolve the neutrino radiation field while keeping the hydrodynamics fixed. After sufficient evolution time has passed, the neutrino radiation fields reach equilibrium. At that point, the difference between the total number of neutrinos entering the grid (through matter interactions) and exiting the grid (through the outer boundary) directly conveys any non-conservation in the evolution equations.

During the late stages of core collapse, both inelastic scattering and energy coupling terms are important and are potential sources of number violation. We examine two specific configurations with central densities of  $\rho_c \sim 10^{11} \text{ g cm}^{-3}$  and  $\rho_c \sim 9 \times 10^{11} \text{ g cm}^{-3}$ . To isolate causes of neutrino number violation, we test these configurations with and without neutrino-electron inelastic scattering. At  $\rho_c \sim 10^{11} \text{ g cm}^{-3}$ , the neutrino number violation is  $\lesssim 0.27\%$  regardless of whether we include inelastic scattering or not. At  $\rho_c \sim 9 \times 10^{11} \text{ g cm}^{-3}$ , the neutrino number violation seen is  $\sim 0.76\%$  and  $\sim 0.53\%$  when including and neglecting neutrino-electron inelastic scattering, respectively.

We also do this test at 100 ms after bounce. We find  $\sim 3\%$  number violation for electron neutrinos regardless of whether we include inelastic scattering or not. This result is consistent with the tests in section §4.2 where we saw that most of the number violation ( $\sim 2\%$  in those tests) is occurring in the optically thick core.

### 5.4. Black Hole Formation

As a final test of our general relativistic neutrino transport code, we evolve a presupernova model with a zero-age main sequence mass of  $40 M_\odot$  to the onset of protoneutron star collapse to a black hole. We use the progenitor model from Woosley & Heger (2007) and the  $K_0 = 220 \text{ MeV}$  variant of the Lattimer & Swesty EOS (LS220) and include the weak magnetism and recoil corrections in our neutrino interaction rates. GR1D evolves to the onset of protoneutron star collapse impressively well considering the strong gravity and relativistic fluid flow. The largest issue we face occurs when the shock

recedes to very small radii and the pre-shock velocity (and its gradient) becomes very large. For example, at 100 ms pre-black hole formation the fluid velocity outside of the shock is  $0.35c$ , the  $g_{rr}$  component of the metric reaches a maximum of 1.7, and the central lapse is 0.5. The explicit energy coupling procedure we have used up to now begins to fail at the shock front. This is understandable as, for example, the average energy of neutrinos in the fluid frame changes by  $\sim 40\%$  across a few zones at the shock front. To aid GR1D in finding the transport solution we switch to an implicit treatment of the energy coupling roughly 100 ms before black hole formation. We also find it necessary to reduce the Courant factor when the simulation approaches black hole formation. The metric of GR1D does not allow the existence of an apparent horizon, and therefore we are unable to evolve past black hole formation, the code stops when the central lapse is  $\sim 0.023$  and the central density has reached  $\sim 3.4 \times 10^{15} \text{ g cm}^{-3}$ . We show the evolution of the neutrino luminosity (left panel) and average energy (right panel) in Fig. 10 from this black hole formation simulation. Unlike in the previous section, here we show the neutrino quantities in the lab frame. The lab frame values are much closer to the asymptotic value than the fluid frame values as the fluid velocity at 500 km is  $\sim 0.1c$ . Since the neutrino radiation takes at least  $t = 500 \text{ km}/c \sim 1.7 \text{ ms}$  to travel from the protoneutron star to the boundary at 500 km, we do not know what the neutrino signal from the final  $\sim \text{ms}$  of evolution is. The post-bounce neutrino luminosities are much higher than the  $15 M_\odot$  model explored in the last section. This is because the post-bounce accretion rate is substantially higher in this progenitor. The qualitative features of the neutrino luminosity and the root mean squared energy match those of Fischer et al. (2009) who used *Agile-BOLTZTRAN* to study black hole formation in a different progenitor (a  $40 M_\odot$  progenitor from Woosley & Weaver 1995) and with a different EOS (LS180, and the H. Shen EOS). The electron neutrino and electron antineutrino luminosities peak at  $\sim 300 \text{ ms}$  after bounce. After this they slowly decline until  $\sim 450 \text{ ms}$  after bounce when the decline steepens. Similar to the  $15 M_\odot$  model from the previous section, this sharp decline is due to the accretion of the silicon-oxygen interface which is located at a baryonic mass coordinate of  $2.34 M_\odot$  and accretes through the shock at this time. Gravitational time dilation and redshift also contribute to this slow decline over the last  $\sim 200 \text{ ms}$ . The evolution of the heavy-lepton neutrino luminosity is more complex since there are several effects coming together. Unlike electron neutrinos and antineutrinos, heavy-lepton neutrino production is not predominately fueled by accretion. It comes from deeper in the protoneutron star and is more analogous to a cooling luminosity. It initially plateaus much earlier ( $\sim 150 \text{ ms}$ ) than the electron type luminosities. Normally, protoneutron star contraction is regulated by cooling and the luminosity slowly declines over time. However, in the case of these extremely massive protoneutron stars with high post-bounce accretion rates, the heavy-lepton neutrino luminosity is driven back up at late times as the matter emitting these neutrinos is not able to cool fast enough via neutrino emission to counteract the compressional heating from gravity and accretion. The same heavy-lepton neutrino luminosity structure is seen in Fischer et al. (2009). The final bump in the heavy-lepton neutrino luminosity is a combination of the drop due to the silicon-oxygen interface accreting in and the rise due to the protoneutron star contraction. As the protoneutron star becomes progressively more massive and compact,

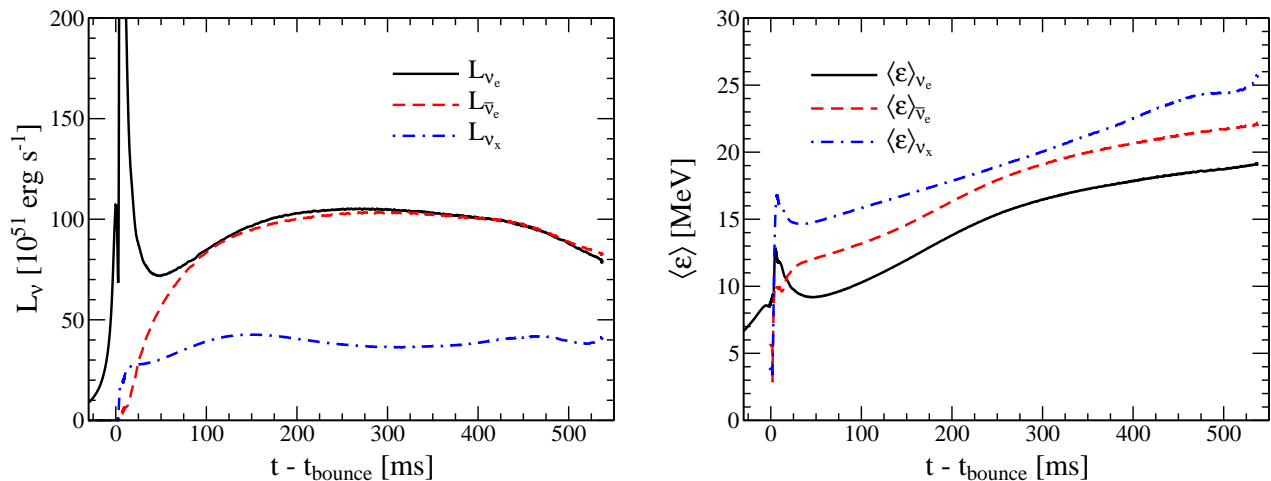


**Figure 10.** Neutrino observables from a failed CCSN simulation of a  $40 M_\odot$  progenitor star from Woosley & Heger (2007) evolved with the LS220 EOS. We show the neutrino luminosity (left panel) and the neutrino average energy (right panel). In both panels, the curves corresponding to electron neutrinos are shown as solid black lines, electron antineutrino curves are shown as dashed red lines, and heavy-lepton neutrino curves are shown as a dashed-dotted blue line. Note the luminosities and average energies presented here are those as measured in the lab frame at 500 km. The lapse function at 500 km is  $\alpha \sim 0.99$ , therefore very little additional redshifting will take place as the neutrinos travel to infinity. This is different than Fig. 6 where the luminosities are measured in the fluid (or comoving) frame for the sake of comparison. In order to compute the neutrino average energy in the lab frame we use the fluid frame value (where the energies are defined) and convert to the lab frame via  $\langle \epsilon \rangle_{\text{lab}} = \langle \epsilon \rangle_{\text{fluid}} W(1+v)$ . Protonneutron star collapse to a black hole occurs at  $\sim 537$  ms, due to the finite neutrino transport time, the last  $\sim 1.7$  ms of the neutrino signal has not yet reached the observer at 500 km.

the neutrino energies also increase.

With GR1D’s neutrino leakage scheme we found a black hole formation time of 561 ms and a maximum protonneutron star gravitational (baryonic) mass of  $\sim 2.31 M_\odot$  ( $\sim 2.44 M_\odot$ ) (O’Connor & Ott 2011). With our neutrino transport methods we find a black hole formation time of  $\sim 537$  ms ( $\sim 24$  ms before the leakage calculation) and a maximum protonneutron star gravitational (baryonic) mass of  $\sim 2.251 M_\odot$  ( $\sim 2.377 M_\odot$ ). These results are remarkably close and confirm our previous work that the progenitor structure, and not details of the neutrino physics, is the determining factor in black hole formation properties (O’Connor & Ott 2011). Our leakage scheme was unable to reliably predict the total neutrino emission. However, with our transport scheme we can make a reliable prediction on the total energy and neutrino number emitted from this particular failed supernova (i.e. for a progenitor matching the  $40 M_\odot$  star from Woosley & Heger (2007) with the LS220 EOS). We find a total neutrino number emission of  $\sim 2.56 \times 10^{57}$ ,  $\sim 2.33 \times 10^{57}$ , and  $\sim 4.03 \times 10^{57}$ , for electron neutrino, electron antineutrino, and all four heavy-lepton neutrinos, respectively. The total energy emission is  $\sim 54.4 \times 10^{51}$  erg,  $\sim 47.6 \times 10^{51}$  erg, and  $\sim 80.6 \times 10^{51}$  erg for electron neutrino, electron antineutrino, and all four heavy-lepton neutrinos, respectively. Summed, this corresponds to  $\sim 182.6 \times 10^{51}$  erg or equivalently  $\sim 0.102 M_\odot$  of mass. The remaining difference between the gravitational mass and the baryonic mass ( $\sim 0.02 M_\odot$ ) was present in the initial progenitor model. We note that while this simulation corresponds to a failed supernova, it only radiates  $\sim 50\%$  of the energy expected to be radiated in successful CCSNe. The rest of the binding energy released during the collapse is still trapped in the matter (either as thermal energy or trapped neutrinos) at the point when the protonneutron star begins its collapse.

## 6. CONCLUSIONS

Neutrinos play a crucial, if not dominant, role in reviving the stalled accretion shock that forms after the iron-core collapse of an evolved massive star. In order to achieve an accurate and self-consistent treatment of neutrinos in core collapse

simulations one has to consider several important aspects of the problem. Deep in the protonneutron star, the mean free path of neutrinos is very small. However, by the time the neutrinos reach 50–130 km, the opacity has decreased enough so that the neutrinos are essentially decoupled from the matter and are free streaming. This transition region is between the optically thick and optically thin region and is very important to capture correctly since it is where the net neutrino heating takes place. Another critical aspect of the problem that must be considered is the strong energy dependence of the neutrino interaction rates. This leads to neutrinos of different energies decoupling at different densities and radii and therefore any self-consistent treatment must be done in an energy dependent way.

For the *hydrodynamic* evolution in the CCSN problem we do not have to deal with these issues because the matter particles are always in thermodynamic equilibrium. We can completely ignore the momentum dependence of the particles (other than the net value) and just solve the hydrodynamic conservation laws for mass, energy, momentum in one, two, or three spatial dimensions (plus time). Since neutrinos in CCSNe are not always in thermodynamic equilibrium, we cannot apply the same techniques for neutrino transport. This makes the symmetry free problem not three dimensional (plus time) but rather a six dimensional problem (plus time). Simulating this six dimensional system at the resolution we need to capture all the essential physics of the CCSN central engine is not feasible with current computational power, so some approximations must still be made. In this paper, we reduced the dimensionality of the problem by removing the angular dependence from the neutrino distribution function and instead evolved moments of the neutrino distribution function—the total energy, and the total momentum. In this sense, our approximation is very much like the approximation made to derive the hydrodynamic equations. The equivalent to the matter pressure is the Eddington tensor. We applied an analytic closure in order to derive this Eddington tensor. We retained the energy dependence of the neutrino distribution function. This reduces the symmetry free problem to four di-

mensions (plus time) and the spherically symmetric problem to two (plus time).

The general-relativistic methodology of this neutrino transport method has recently been presented in Shibata et al. (2011) and Cardall et al. (2013). We presented in this paper the spherically symmetric equivalent in the metric and notation of GR1D. Rather than focus on the derivation of the transport method itself (which is more than adequately presented in both Shibata et al. 2011 and Cardall et al. (2013)), we focused on the numerical implementation in spherical symmetry with the aim of developing methods that will carry over well to multiple dimensions and parallel environments. We presented simple radiation test cases to show our code is correctly modeling transport phenomena in the general relativistic regime. We also showed that our explicit treatment of the spatial flux works well in the diffusion limit, which permitted us to forgo large and computationally expensive matrix inversions. This will be a crucial advantage for multidimensional simulations. We also performed a CCSN simulation following the established standard of Liebendörfer et al. (2005); Marek et al. (2006); Müller et al. (2010). The excellent agreement across many quantities assures us that the neutrino transport, and its coupling to the hydrodynamics is correctly implemented. We tested several approximations that will make the transition from spherically symmetric simulations to multidimensional simulations easier by removing the need to invert large matrices. The accuracy cost of these approximations is very little and within the differences seen in various codes.

As a final test, we followed the evolution of a  $40M_{\odot}$ , solar metallicity progenitor from the onset of core collapse, through bounce to black hole formation. This was an especially stringent test of the robustness of the transport scheme as the spacetime curvature becomes strong near the end of the simulation. Furthermore, the pre-shock velocities reached in the late stages approached  $0.5c$ , much larger than typical CCSNe. The black hole formation time and the black hole birth mass agreed closely with results using a neutrino leakage scheme. While no direct comparison can be made, the evolution of the neutrino quantities qualitatively agrees with other neutrino transport code studying similar progenitors with similar EOS.

In the interest of open-science, ensuring reproducibility, full disclosure, and to provide technology for other scientific researchers, all of our code is open-source. The neutrino transport methods are included as an update to GR1D and are available as a git repository at [www.GR1Dcode.org](http://www.GR1Dcode.org). All of the neutrino microphysics comes from the open-source neutrino interaction library NuLib, also available as a git repository <http://www.nulib.org>. Both repositories have a tagged released named ‘GR1Dv2’. We make the NuLib tables used for our core collapse simulations in this paper as well as the parameter files and scripts needed to generate the data in this paper available at [www.stellarcollapse.org/GR1Dv2](http://www.stellarcollapse.org/GR1Dv2).

#### ACKNOWLEDGEMENTS

The author would like to thank Francois Foucart and Luke Roberts for many in depth discussions surrounding this topic, Matthias Liebendörfer for discussions regarding Liebendörfer et al. (2005), and the referee for helpful comments that have improved the manuscript. Furthermore, for productive and helpful discussions we acknowledge Adam Burrows, Christian Cardall, Sean Couch, Thomas Janka, Anthony Mezza-

cappa, Bernhard Mueller, and Chris Sullivan. The author would like to especially thank Christian Ott for his advisement during the first part of this work and for a careful reading of this manuscript. Computations were performed on the Zwicky cluster at Caltech, which is supported by the Sherman Fairchild Foundation and by NSF award PHY-0960291. Part of this research performed at Caltech was supported by AST-1212170 and AST-0855535. Support for this work was provided by NASA through Hubble Fellowship grant #51344.001-A awarded by the Space Telescope Science Institute, which is operated by the Association of Universities for Research in Astronomy, Inc., for NASA, under contract NAS 5-26555.

#### REFERENCES

- Abdikamalov, E., Burrows, A., Ott, C. D., Löffler, F., O’Connor, E., Dolence, J. C., & Schetter, E. 2012, *ApJ*, 755, 111
- Antoniadis, J., Freire, P. C. C., Wex, N., Tauris, T. M., Lynch, R. S., van Kerkwijk, M. H., Kramer, M., Bassa, C., Dhillon, V. S., Driebe, T., Hessels, J. W. T., Kaspi, V. M., Kondratiev, V. I., Langer, N., Marsh, T. R., McLaughlin, M. A., Pennucci, T. T., Ransom, S. M., Stairs, I. H., van Leeuwen, J., Verbiest, J. P. W., & Whelan, D. G. 2013, *Science*, 340, 448
- Audit, E., Charrier, P., Chièze, J., & Dubroca, B. 2002, arXiv:0206281
- Bethe, H. A. 1990, *Rev. Mod. Phys.*, 62, 801
- Bethe, H. A., & Wilson, J. R. 1985, *ApJ*, 295, 14
- Brandt, T. D., Burrows, A., Ott, C. D., & Livne, E. 2011, *ApJ*, 728, 8
- Bruenn, S. W. 1985, *ApJS*, 58, 771
- Buras, R., Janka, H.-T., Rampp, M., & Kifonidis, K. 2006a, *A&A*, 457, 281
- Buras, R., Rampp, M., Janka, H.-T., & Kifonidis, K. 2006b, *A&A*, 447, 1049
- Burrows, A. 2013, *Rev. Mod. Phys.*, 85, 245
- Burrows, A., Hayes, J., & Fryxell, B. A. 1995, *ApJ*, 450, 830
- Burrows, A., Livne, E., Dessart, L., Ott, C. D., & Murphy, J. 2007, *Astrophys. J.*, 655, 416
- Burrows, A., Reddy, S., & Thompson, T. A. 2006, *Nuclear Physics A*, 777, 356
- Burrows, A., Young, T., Pinto, P., Eastman, R., & Thompson, T. A. 2000, *ApJ*, 539, 865
- Cardall, C. Y., Endeve, E., & Mezzacappa, A. 2013, *Phys. Rev. D*, 87, 103004
- Chernohorsky, J. 1994, *ApJ*, 433, 247
- Colella, P., & Woodward, P. R. 1984, *J. Comp. Phys.*, 54, 174
- Demorest, P. B., Pennucci, T., Ransom, S. M., Roberts, M. S. E., & Hessels, J. W. T. 2010, *Nature*, 467, 1081
- Einfeldt, B. 1988, in *Shock tubes and waves; Proceedings of the Sixteenth International Symposium, Aachen, Germany, July 26–31, 1987*. VCH Verlag, Weinheim, Germany, 671
- Fischer, T., Whitehouse, S. C., Mezzacappa, A., Thielemann, F.-K., & Liebendörfer, M. 2009, *A&A*, 499, 1
- , 2010, *A&A*, 517, A80
- Font, J. A., Miller, M., Suen, W.-M., & Tobias, M. 2000, *Phys. Rev. D*, 61, 044011
- Fryer, C. L. 1999, *ApJ*, 522, 413
- Gourgoulhon, E. 1991, *A&A*, 252, 651
- Herant, M., Benz, W., Hix, W. R., Fryer, C. L., & Colgate, S. A. 1994, *ApJ*, 435, 339
- Horowitz, C. J. 1997, *Phys. Rev. D*, 55, 4577
- , 2002, *Phys. Rev. D*, 65, 043001
- Hüdepohl, L., Müller, B., Janka, H.-T., Marek, A., & Raffelt, G. G. 2010, *Phys. Rev. Lett.*, 104, 251101
- Janka, H.-T. 1992, *A&A*, 256, 452
- , 2012, *Ann. Rev. Nuc. Par. Sci.*, 62, 407
- Janka, H.-T., & Hillebrandt, W. 1989a, *A&AS*, 78, 375
- , 1989b, *A&A*, 224, 49
- Janka, H.-T., Langanke, K., Marek, A., Martínez-Pinedo, G., & Müller, B. 2007, *Phys. Rep.*, 442, 38
- Jin, S., & Levermore, C. D. 1996, *J. Comp. Phys.*, 126, 449
- Just, O., Obergaulinger, M., & Janka, H.-T. 2015, ArXiv e-prints arXiv:1501.02999
- Kuroda, T., Kotake, K., & Takiwaki, T. 2012, *ApJ*, 755, 11
- Kuroda, T., Takiwaki, T., & Kotake, K. 2015, ArXiv e-prints
- Langanke, K., Martínez-Pinedo, G., Sampaio, J. M., Dean, D. J., Hix, W. R., Messer, O. E., Mezzacappa, A., Liebendörfer, M., Janka, H.-T., & Rampp, M. 2003, *Phys. Rev. Lett.*, 90, 241102

- Lattimer, J. M., & Swesty, F. D. 1991, *Nucl. Phys. A*, 535, 331
- Lentz, E. J., Mezzacappa, A., Bronson Messer, O. E., Hix, W. R., & Bruenn, S. W. 2012, *ApJ*, 760, 94
- Liebendörfer, M. 2015, Private communication
- Liebendörfer, M., Messer, O. E. B., Mezzacappa, A., Bruenn, S. W., Cardall, C. Y., & Thielemann, F.-K. 2004, *ApJS*, 150, 263
- Liebendörfer, M., Rampp, M., Janka, H.-T., & Mezzacappa, A. 2005, *ApJ*, 620, 840
- Liebendörfer, M., Whitehouse, S. C., & Fischer, T. 2009, *ApJ*, 698, 1174
- Lindquist, R. W. 1966, *Annals of Physics*, 37, 487
- Livne, E., Burrows, A., Walder, R., Lichtenstadt, I., & Thompson, T. A. 2004, *ApJ*, 609, 277
- Marek, A., Dimmelmeier, H., Janka, H.-T., Müller, E., & Buras, R. 2006, *A&A*, 445, 273
- Mezzacappa, A., & Bruenn, S. W. 1993a, *ApJ*, 405, 669
- . 1993b, *ApJ*, 410, 740
- . 1993c, *ApJ*, 405, 637
- Minerbo, G. N. 1978, *J. Quant. Spec. Radiat. Transf.*, 20, 541
- Müller, B., & Janka, H.-T. 2015, *MNRAS*, 448, 2141
- Müller, B., Janka, H.-T., & Dimmelmeier, H. 2010, *ApJS*, 189, 104
- Obergaulinger, M., Janka, H.-T., & Aloy, M. A. 2014, *MNRAS*, 445, 3169
- O'Connor, E., & Ott, C. D. 2010, *Class. Quantum Grav.*, 27, 114103
- . 2011, *ApJ*, 730, 70
- . 2013, *ApJ*, 762, 126
- Ott, C. D., Burrows, A., Dessart, L., & Livne, E. 2008, *ApJ*, 685, 1069
- Perego, A., Rosswog, S., Cabezón, R. M., Korobkin, O., Käppeli, R., Arcones, A., & Liebendörfer, M. 2014, *MNRAS*, 443, 3134
- Pons, J. A., Ibáñez, J. M., & Miralles, J. A. 2000, *MNRAS*, 317, 550
- Rampp, M., & Janka, H.-T. 2002, *A&A*, 396, 361
- Reddy, S., Prakash, M., & Lattimer, J. M. 1998, *Phys. Rev. D*, 58, 013009
- Roberts, L. 2014, private communication
- Roberts, L. F. 2012, *ApJ*, 755, 126
- Romero, J. V., Ibanez, J. M., Marti, J. M., & Miralles, J. A. 1996, *ApJ*, 462, 839
- Rosswog, S., & Liebendörfer, M. 2003, *MNRAS*, 342, 673
- Ruffert, M., Janka, H.-T., & Schäfer, G. 1996, *A&A*, 311, 532
- Scheck, L., Kifonidis, K., Janka, H.-T., & Müller, E. 2006, *A&A*, 457, 963
- Sekiguchi, Y. 2010, *Class. Quantum Grav.*, 27, 114107
- Shibata, M., Kiuchi, K., Sekiguchi, Y., & Suwa, Y. 2011, *Prog. Theor. Phys.*, 125, 1255
- Smit, J. M., Cernohorsky, J., & Dullemond, C. P. 1997, *A&A*, 325, 203
- Sumiyoshi, K., Takiwaki, T., Matsufuru, H., & Yamada, S. 2015, *ApJS*, 216, 5
- Sumiyoshi, K., & Yamada, S. 2012, *ApJS*, 199, 17
- Sumiyoshi, K., Yamada, S., Suzuki, H., Shen, H., Chiba, S., & Toki, H. 2005, *ApJ*, 629, 922
- Swesty, F. D., & Myra, E. S. 2009, *ApJS*, 181, 1
- Thompson, T. A., Burrows, A., & Pinto, P. A. 2003, *ApJ*, 592, 434
- van Leer, B. J. 1977, *J. Comp. Phys.*, 23, 276
- Woosley, S. E., & Heger, A. 2007, *Phys. Rep.*, 442, 269
- Woosley, S. E., & Weaver, T. A. 1995, *ApJS*, 101, 181
- Yakunin, K. N., Marronetti, P., Mezzacappa, A., Bruenn, S. W., Lee, C.-T., Chertkow, M. A., Hix, W. R., Blondin, J. M., Lentz, E. J., Bronson Messer, O. E., & Yoshida, S. 2010, *Class. Quantum Grav.*, 27, 194005
- Yamada, S. 1997, *ApJ*, 475, 720
- Yueh, W. R., & Buchler, J. R. 1976, *Ap&SS*, 41, 221
- Zhang, W., Howell, L., Almgren, A., Burrows, A., Dolence, J., & Bell, J. 2013, *ApJS*, 204, 7